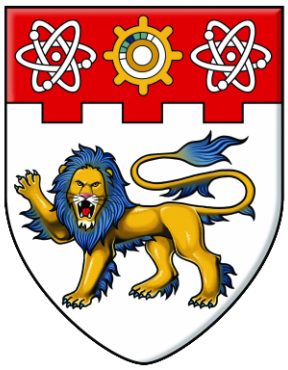

NANYANG TECHNOLOGICAL UNIVERSITY

PHOTOVOLTAIC PROPERTY OF BISMUTH FERRITE THIN FILMS AND ITS APPLICATION AS NON-VOLATILE PHOTOVOLTAIC FERAM

PHOTOVOLTAIC PROPERTY OF BISMUTH FERRITE THIN FILMS AND ITS APPLICATION IN NON-VOLATILE MEMORY

GUO RUI

SCHOOL OF MATERIALS SCIENCE AND ENGINEERING

2013

GUO RUI

2013

PHOTOVOLTAIC PROPERTY OF BISMUTH FERRITE THIN FILMS AND ITS APPLICATION IN NON-VOLATILE MEMORY

Guo Rui

School of Materials Science and Engineering

A thesis submitted to the Nanyang Technological University

in fulfillment of the requirement for the degree of

Doctor of Philosophy

2013

ACKOWLEGEMENT

First of all, I would like to convey my deepest gratitude to my supervisor, associate professor Wang Junling, for his guidance in my research work during my PhD period. Prof. Wang is an amazing supervisor, who is not only knowledgeable, but also very helpful to students. His profound knowledge and preciseness in science enlighten me really a lot. I benefited greatly from his inspiring ideas, suggestions and the discussions we had. Moreover, during the four years, I have learnt not only how to do research, but also how to do things. The serious attitude plus the correct smart ways to do things will make me not afraid of difficulty in my future life. All of these that I have learnt from Prof. Wang will be a great wealth for the rest of my life.

Here, I also take the opportunity to thank another amazing professor, my former supervisor, Yang Jianfeng, who keeps helping and encouraging me all the time. What I have learnt from Prof. Yang and his help to me benefit me forever.

Secondly, I wish to extend my thanks to all my current and former groupmates. Dr. You Lu (our best group leader), Dr. Zou Xi, Dr. Zheng Zhaoke, Dr. Wang Baomin, Dr. Ong Hock Guan, Dr. Chen Weigang, Dr. Zhang Zhen, Dr. Yang Pan, Dr. Chen Zuhuang, Dr. Rami, Dr. Chua Ngeah Theng, Dr. Wang Yang, Dr. Dr. Suresh Kumar, Mr. Lim Zhishuish, Mr. Zhou Yang, Mr. Jason, Ms. Ding Hui, and so on. All my groupmates are so nice to me. It's very comfortable to work in my group. It's like a family. All my dear friends, your suggestions and encouragement are indispensable in my life.

Here, I also want to thanks Prof. Chen Lang for his engorgements and suggestions in my project. Thank the technicians and collaborators from other groups for their help.

Thirdly, I thank my best friends, Chen Xi, Ding Mingwang, Wei Deyuan, Xu Luxiang, Zhou Haiping, Dong Li, Zhang Juan... The friendship makes my PhD life full and colorful.

Last but not least, I would like to give the special thanks to my fiancé Chandra Nugraha, and my family. Your love and support are all the motivations in my progress.

TABLE OF CONTENTS

LIST OF FIGURES

LIST OF TABLES

ABSTRACT

In conventional junction-based photovoltaic cells, the photovoltage is usually smaller than the semiconductor band gap, due to the limitation of the energy barrier at the interface. Contrarily, ferroelectric photovoltaic effect is a bulk effect of which the photovoltage is not limited by the energy barrier. Therefore, ferroelectric photovoltaic effect has attracted much research attention due to its wide potential applications. $BiFeO_3$, a multiferroic material with robust ferroelectric and magnetic orders at room temperature[1] and a band gap within visible light range[2], provides a unique opportunity for bulk photovoltaic effect study. Earlier work on $BiFeO_3$ photovoltaic property attributed the effect mainly to the ferroelectric polarization. However, a very large photovoltage was reported later in $BiFeO_3$ films with regular 71° domains.[3] The authors proposed that the effect arises from the electrostatic potential steps at the domain walls. Moreover, $BiFeO_3$ films with regular 109° domain walls are expected to generate a significantly larger photovoltage, since the potential step at 109° domain walls was reported to be much larger than that at 71° domain walls.[4] This project thus aimed to study the photovoltaic effect of $BiFeO_3$ films with regular 109° domains, in order to clarify its correlation with the domain wall. To achieve this, we set our goal to control the domain structure of $BiFeO_3$ thin films first. In fact, the ability to control domain structure is an essential work for various research topics. Ferroelectric domain walls in $BiFeO_3$ have been shown to possess unique properties that do not exist in bulk material. Theoretical studies have predicted that a net electric field or magnetic moment could in principle exist in the center of domain walls while the domain themselves were non-electric or non-magnetic. However, a systematic investigation requires the precise control of domain structures in $BiFeO_3$, which is still lacking. In this project the underlying mechanism of domain engineering will be addressed. Then, the photovoltaic effect of $BiFeO_3$ films with regular 109° domains will be studied. The correlation of the photovoltaic effect with the domain walls will be discussed. Finally, after this, we studied the application of the photovoltaic effect of $BiFeO_3$ films in memory device. The photovoltaic effect could be used to read the polarization status of $BiFeO_3$ films non-destructively. The properties of the memory cells were studied and compared with other technologies.

Pulsed Laser Deposition technique was used to grow $BiFeO_3$ films. By using $BiFeO_3$ target with different Bi content or adjusting the deposition parameters, films with regular 71° to 109° domains can be obtained. The domain structure was tested by Piezoelectric Force Microscopy, and the thin film composition was measured using Electron Probe X-ray Micro-analyzer. It is revealed that decreasing Bi content in the target or increasing substrate temperature changes the domain structure of $BiFeO_3$ from 71° to 109°. Domain structure is related to the Bi vacancies in the thin film. We suggest that a combination of interface effect and defect induced internal field causes this evolution.

After the successful control of domain structure in $BiFeO_3$ thin films, the photovoltaic property of $BiFeO_3$ thin films with 109° domains was studied. $BiFeO_3$ thin films that contain regular 109° domains with mainly two polarization variants were prepared by using miscut $DyScO_3$ substrates. A direct correlation between the 109° domains switching and the photovoltaic response of the films was established, by conducting piezoelectric force microscopy study using a planar device. The polarity of the photovoltage is switchable upon polarization reversal. Besides, the photovoltage was also obtained in single domain $BiFeO_3$ thin films. The results suggest that theoretical study might have overestimated the contribution of domain walls to $BiFeO_3$ photovoltaic effect.

After the study of the photovoltaic effect of $BiFeO_3$ thin films, we investigated the possibility of using ferroelectric photovoltaic effect in non-volatile memory. Capacitors of Fe/$BiFeO_3$ /$(La_{0.7},Sr_{0.3})MnO_3$ were prepared on miscut $SrTiO_3$ substrates. Photovoltage and photocurrent with opposite signs were obtained upon switching the polarization of the capacitor. The stored polarization information in $BiFeO_3$ could be read non-destructively by sensing the photovoltage or photocurrent. The memory performance such as write energy, operation speed, retention time and fatigue cycles compare favorably with other memories, such as hard disk drive, flash memory, magnetoresistive random access memory and resistive switching random access memory.

Chapter 1 Introduction

1.1 Conventional and ferroelectric photovoltaic effect

Conventional photovoltaic cells are based on p-n or Schottky junctions. Under illumination, photons with energy higher than the semiconductor band gap are absorbed to generate electron-hole pairs, which are then separated by the internal field. The internal electric field is generated by the band bending which spans over a micrometer-thick depletion region. Consequently, the photovoltage is limited by the energy barrier height at the interface region and is always smaller than the semiconductor band gap.[5, 6] Figure 1.1 shows the working mechanism of a p-n junction photovoltaic cell.

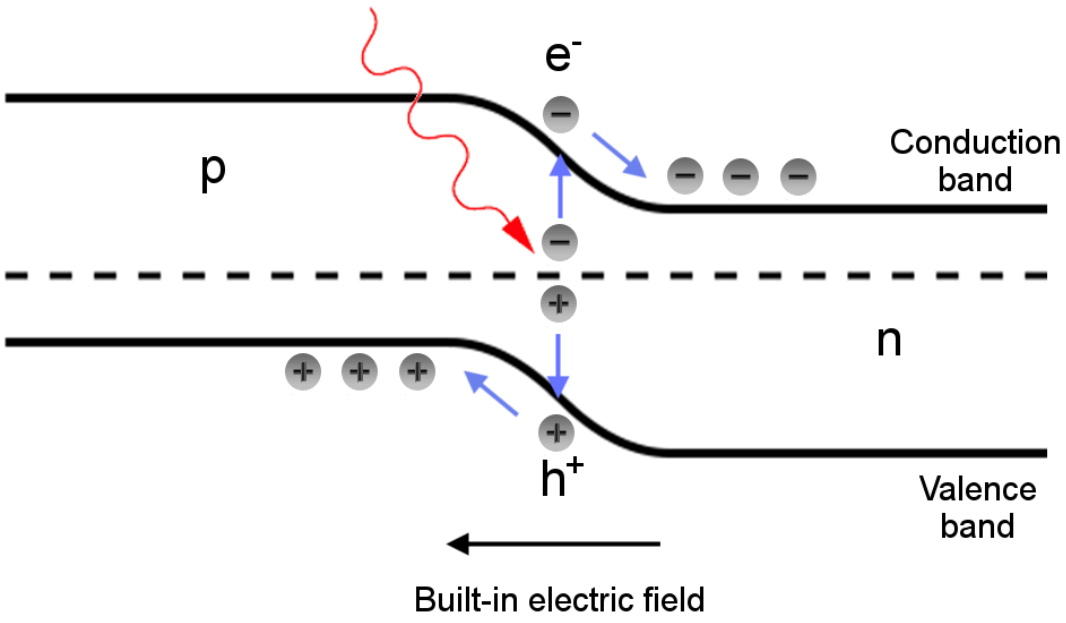

Figure 1.1 Working mechanism of a p-n junction solar cell. The built-in electric field which exists in the interfacial area separates the electron-hole pairs generated under illumination.

Besides the conventional p-n or Schottky junctions, there are other pathways to achieve charge separation in materials. For example, steady-state photocurrent has been observed in homogeneous ferroelectric materials under illumination, which is named ferroelectric photovoltaic effect. Since its discovery in $BaTiO_3$ in 1956,[7] much research has been done on this topic. Although the physical mechanism of photovoltaic effect in ferroelectrics has not been fully clarified, it is certainly related to the ferroelectric polarization.[8-14] Different from the internal field in conventional junction-based photovoltaic cells, the polarization induced internal field extends over the whole ferroelectrics. Therefore, ferroelectric photovoltaic effect is mainly a bulk effect. Abnormally large photovoltage has been reported. For example, a large photovoltage of 7 V was reported for $Pb_{0.97}La_{0.03}(Zr_{0.52}Ti_{0.48})O_3$ ferroelectric thin film with planar structure under ultraviolet light illumination.[11] Figure 1.2 shows the possible mechanism of ferroelectric photovoltaic effect. The switchable photovoltaic effect was explained by the polarization dependent band modification of the $BiFeO_3$ (BFO) capacitor. The unscreened polarization charge bends the electronic band and thus generates the built-in electric field of which the direction depends on the polarization direction. When incident light energy is above the band gap of the material, electron-hole pairs will be generated and then be separated by the built-in electric field. For ferroelectric photovoltaic effect, besides the polarization-induced internal field, other factor such as the Schottky barriers at the interfaces between the ferroelectric material and the electrodes should also be taken into consideration. The Schottky barrier also generates an internal field, which will contribute to the photovoltaic effect.[9, 10, 15] For the sandwiched structure, the Schottky barriers at the two ferroelectric-electrode interfaces are usually different even with the same

electrodes due to different processing conditions. It adds a non-switchable internal field to the overall response. Therefore, the *I-V* curves with opposite polarization states under light illumination are not symmetric.[9]

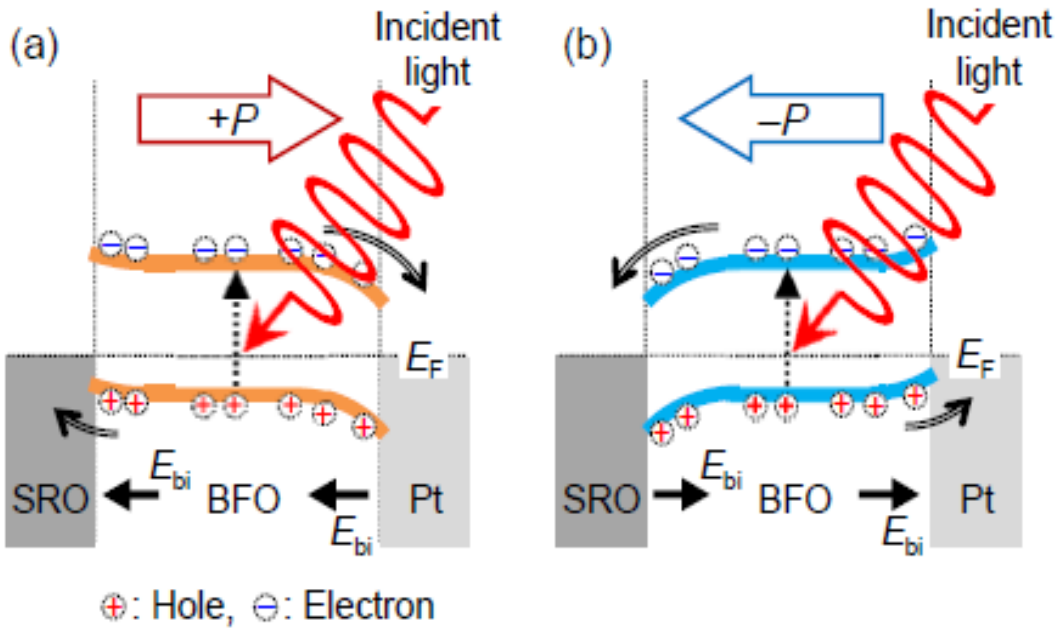

Figure 1.2 Schematic of photovoltaic mechanism in ferroelectric thin film. Figure adapted from [16]. (a) The upward polarization with downward built-in electric field and (b) the downward polarization with upward built-in electric field.

Ferroelectric photovoltaic effect has attracted much attention because of its potential applications for optical detection[17], wireless actuation in microelectromechanical systems (MEMS)[18, 19], optical information storage[20], and photovoltaic devices[21]. Previous studies mainly focused on $BaTiO_3$ and $Pb(ZrTi)O_3$, whose band gaps are in the UV region. BFO, a multiferroic material with robust ferroelectric and magnetic orders at room temperature[1] and a band gap (~ 2.7 eV) within visible light range[2], provides a unique opportunity for ferroelectric photovoltaic effect study and applications.

1.2 Previous work on $BiFeO_3$

Up to now, BFO is the only known single phase material with robust ferroelectric (Curie temperature ~1103 K)[22] and magnetic (Neél temperature ~643 K)[23] orders coexisting at room temperature. Furthermore, it is environmentally friendly and has a relatively simple perovskite structure. Therefore, it has been intensively studied both experimentally and theoretically.

1.2.1 Physical Properties of Multiferroic $BiFeO_3$

1.2.1.1 Crystal structure of $BiFeO_3$

At room temperature, BFO has a rhombohedral (point group *R*3*c*) structure.[24] Its crystal structure is characterized by two highly distorted perovskite units connected along their body diagonal direction, denoted as pseudocubic $<111>_{pc}$ [25], as shown in figure 1.3. At room temperature, the pseudocubic unit cell has a lattice parameter (α_{rh}) of 3.965 Å, and a rhombohedral angle of ca. 89.3-89.4°.[24] The large displacement of the Bi ions relative to the FeO_6 octahedra gives rise to a large spontaneous polarization along the $<111>_{pc}$ direction.[26, 27] As a result, there are totally eight possible polarization directions which correspond to four structural variants.

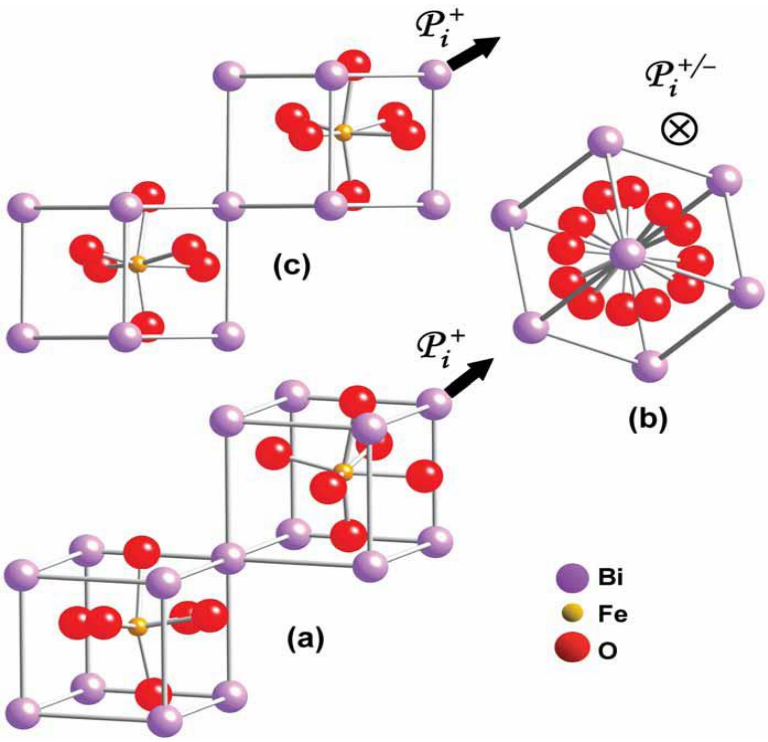

Figure 1.3 (a)-(c) Crystal structure of (001) BFO viewing from different directions. Figure adapted from [28].

1.2.1.2 Ferroelectricity of $BiFeO_3$

Early measurement of the polarization of BFO in the 1970s yielded a value of only ~6 μC/cm^2 along <111>$_{pc}$ directions.[22] The small value of remnant polarization (P_r) was viewed as limited by the lack of saturation. In 2003, Wang *et al.*[1] reported large polarization in $(001)_{pc}$ epitaxial BFO thin film, corresponding to ~100 μC/cm^2 in $(111)_{pc}$ direction, consistent with the theoretical calculations[29]. This discovery spurred intense research focusing on BFO in various forms. The enhancement of polarization was assumed to be due to strain from substrate. Recently, high quality BFO single crystals reveal polarization value similar to those of epitaxial thin films, unveiling the intrinsic nature of the large polarization rather than the originally proposed epitaxial strain induced extrinsic effect.[30, 31] Strain dependent studies[32, 33] together with the theoretical

calculation[29] also suggest that the intrinsic polarization of BFO epitaxial films is actually insensitive to strain. Ferroelectric hysteresis loops of epitaxial BFO films with different crystallographic orientations are shown in figure 1.4. The remnant polarization of BFO thin film on (100) substrate is around 65 μC/cm^2, which reaches 100 μC/cm^2 when grown on (111) oriented substrate.

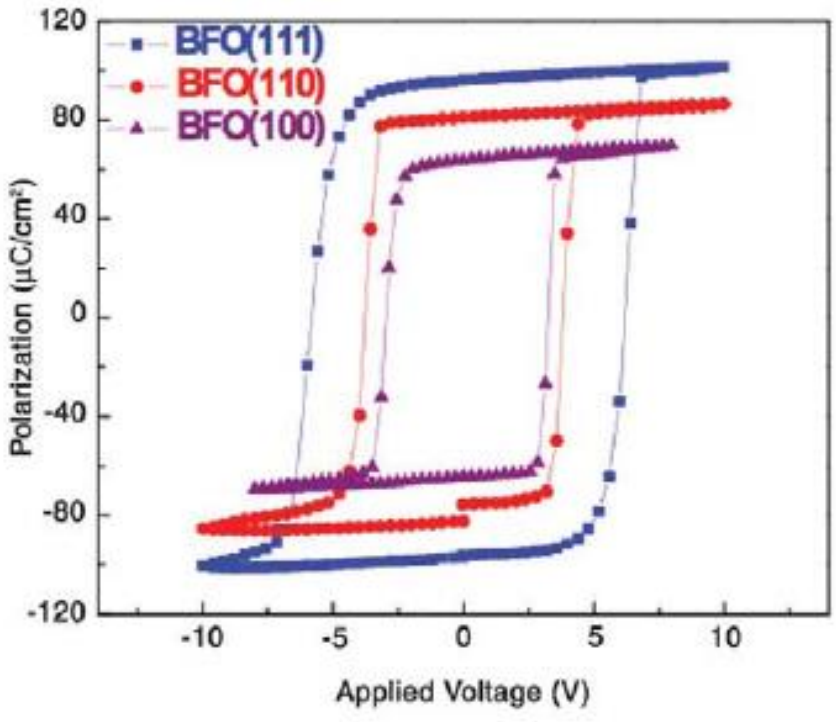

Figure 1.4 Ferroelectric hysteresis loops of epitaxial BFO films with different crystallographic orientations. Figure adapted from [34].

1.2.1.3 Magnetic property of $BiFeO_3$

BFO has a G-type antiferromagnetic structure. As shown in figure 1.5, each Fe^{3+} magnetic moment is surrounded by six antiparallel moments of the nearest Fe^{3+} neighbors. In another word, the Fe^{3+} magnetic moments are coupled ferromagnetically within the pseudocubic $(111)_{pc}$ planes and antiferromagnetically between adjacent planes.

In bulk BFO, the orientation of the antiferromagnetic vector follows a cycloidal spiral with a long period of 620 ± 20 Å, where $[110]_{pc}$ is the spiral direction and $(110)_{pc}$ is the spin rotation plane.[35, 36] Although there is canting of spins, the net magnetic moment in bulk BFO is zero since it follows the spiral structure. For BFO thin films, there is no spin cycloid due to symmetry breaking induced by epitaxial strain. BFO thin films thus have a weak magnetic moment which is generated by the canting. The weak canting is caused by the local magnetoelectric coupling,[37] which leads to a small net magnetic moment. However, magnetization of BFO thin films caused by the small canting is very small. A significant enhancement of the magnetization (~0.5 μ_B/Fe) was reported originally by *Wang et al*.[1], and later study suggested that the enhanced magnetization may be correlated with the valence change of Fe ions or magnetic second phases.[38, 39]

First principles calculations of the magnetocrystalline anisotropy energy show that the preferred orientation of the individual magnetic moment is perpendicular to the rhombohedral axis.[40] There is a six-fold degeneracy within the corresponding $(111)_{pc}$ plane, resulting in an effective 'easy magnetization plane' for the magnetic moments. The easy magnetization plane is always perpendicular to the ferroelectric polarization and coupled to the ferroelectric/ferroelastic strain state. Consequently, ferroelectric polarization switching by either 71º or 109º will change the orientation of the easy magnetization plane.[41] The electric field control of magnetization at room temperature through the coupling between multiferroic BFO and a ferromagnet CoFe was reported recently,[42] making BFO an ideal candidate for future magnetoelectric random access memory.[43]

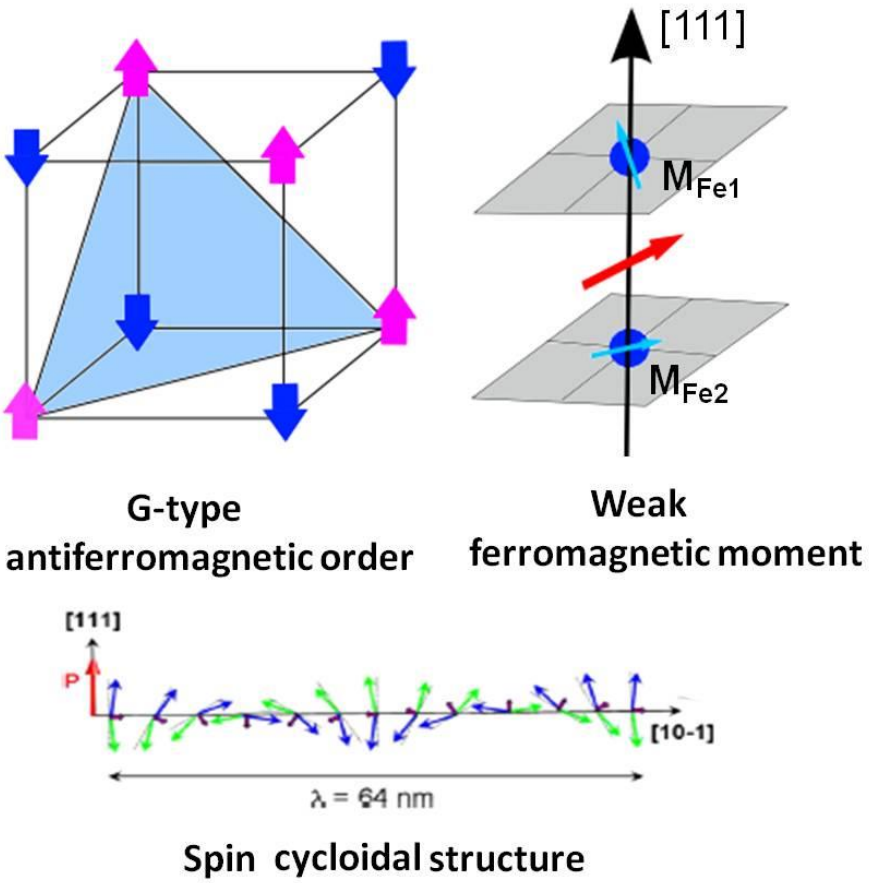

Figure 1.5 Magnetic structure of BFO. Figure adapted from [37].

1.2.1.4 Ferroelectric domain structure of $BiFeO_3$

In ferroelectrics, domain structures form to release the elastic/electrostatic energy at the expense of increased interfacial energy at the domain boundaries.[44, 45] Bulk BFO has a rhombohedral structure, and its polarization points along one of the body diagonal directions. When BFO is epitaxially grown on substrates, the rhombohedral symmetry is reduced to monoclinic with the distortion along $<111>_{pc}$ direction, due to the epitaxial strain. Therefore, there are totally four ferroelastic structural variants which correspond to eight polarization variants as shown in figure 1.6. These eight polarization variants can form three types of domain walls (71°, 109°, and 180°) depending on the angles between the adjacent polarization variants. For example, polarization P_1^+ and P_2^+ form a 71°

domain wall, polarization P_1^+ and P_2^- form a 109º domain wall, and polarization P_1^+ and P_1^- form a 180º domain wall.

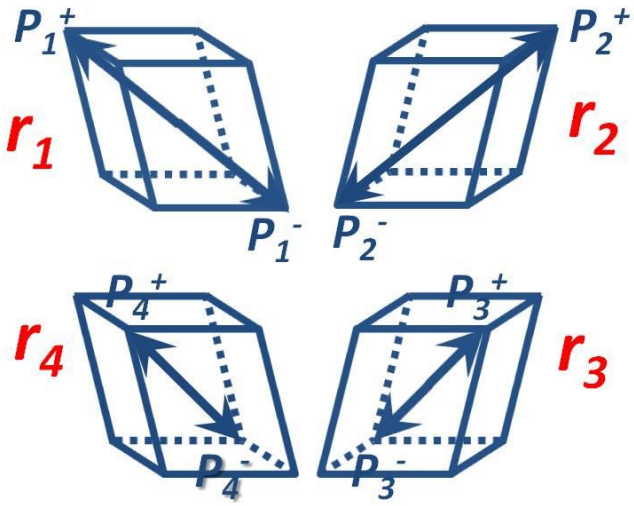

Figure 1.6 Schematic of the four structural variants and corresponding eight polarization variants in **BFO** thin film.

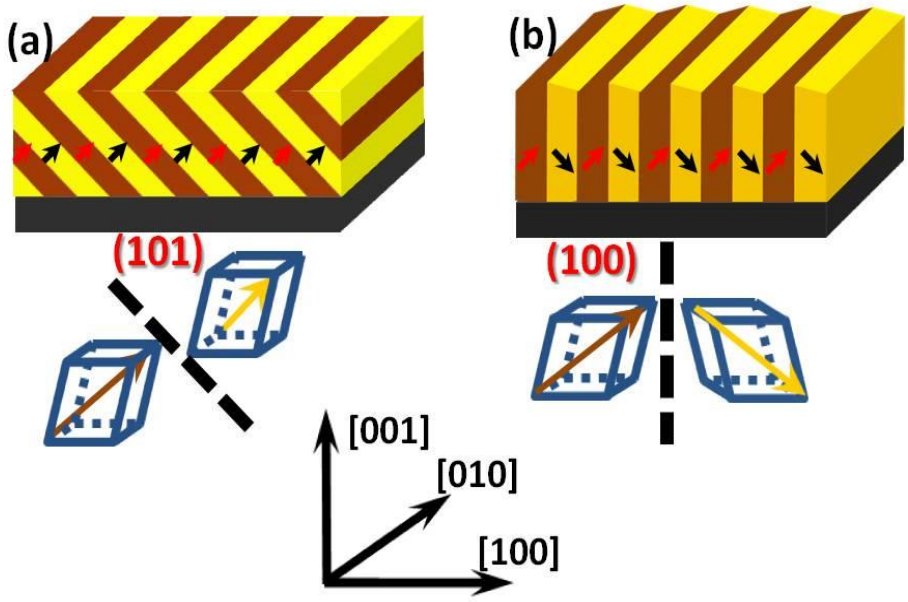

Figure 1.7 Schematic of (a) 71° and (b) 109° domain patterns in BFO thin films.

Domain structures depend on the substrate, substrate orientation, and the deposition parameters. Domain patterns in epitaxial BFO ferroelectric thin films could be predicted

according to the theory proposed by Streiffer *et al*. [45] For BFO thin films on the (001) oriented substrates, the four structural variants are energetically degenerate, and therefore have the equal chance to exist in the film. The combination of different polarization variants can lead to complicate domain structures. Possible domain walls are decided by both mechanical and charge compatibility. To satisfy the mechanical requirement, domain patterns may form with either {100} or {101} boundaries (to release strain energy), corresponding to 109^{o} and 71^{o} domain patterns, respectively. On the (001) substrate, 109^{o} domain patterns have a puckered fashion on the topography, while 71^{o} domain patterns have a flat topography, as shown in figure 1.7. Charge compatibility must be satisfied to achieve neutral charge at the domain boundaries. Therefore, 109^{o} patterns must have the opposite out-of-plane (OOP) component of polarization in adjacent domains, while charge neutrality for 71^{o} domains can only be obtained when all domains have the same OOP component of polarization, as shown in figure 1.7. If we consider the total net polarization of the film, the alternating OOP components of polarization in 109° domain patterns will cancel each other out, and thus reduce the depolarization field; while the same OOP components of polarization in 71^{o} domain patterns lead to a finite component in the substrate normal direction, corresponding to a fully-poled state. As a consequence, the fully-poled state 71^{o} domains have a large depolarization field in the film which needs to be balanced to make the domains stable. To sum up, 71^{o} domains have {101} type domain walls with a flat topography on (001) surface, and all domains have the same OOP polarization component, corresponding to fully-poled state; while 109^{o} domains have {100} type domain walls with a puckered fashion of topography, and the adjacent domains have opposite OOP polarization component, lending to no normal

component of the net polarization. And for the 180° domain walls, they don't need to follow any specific crystallographic planes, because 180º domains are ferroelectric rather than ferroelastic, there is no elastic constraint on the domain wall.

For a BFO thin film grown on (001) oriented $SrTiO_3$ (STO) substrate, individual domains are energetically degenerate. So four structural variants have the equal chance to appear, and twinning domain patterns are expected to form to release the elastic energy in the film. However, experimentally, BFO films on STO substrates are in a fully poled state, only the upward polarization variants are observed. Some studies suggest that it is due to the oxygen vacancies.[46, 47] As for BFO thin films on (110) and (111) oriented substrates, their domain patterns are relatively simple. For BFO thin films on (110) oriented STO substrate, the compressive strain will drive the polarization towards the OOP direction, and thus favors only two out of the four structural variants. For BFO films on (111) STO substrates, under compressive strain, only the polarization variants perpendicular to the film surface is energetically stable. Therefore, therefore the structural variants are further reduced to one, corresponding to a single domain state.[34] The ferroelectric domain structure can be revealed by using piezoelectric force microscopy (PFM), which will be explained in details in chapter 2.

The dynamic polarization switching process has also been investigated using PFM. All three possible switching mechanisms (namely 71°, 109° and 180° switching) have been observed. The 71°, 109° switching are accompanied by the change of structure distortion, thus being ferroelastic in nature, whereas 180° switching is purely ferroelectric. 180°

polarization reversal seems to be the most favorable switching mechanism in epitaxial films under an applied field along $[001]_{pc}$.[41]

1.2.2 Domain wall functionalities and the control of domain structures in $BiFeO_3$ thin films

Domain walls exist in many materials that possess certain order parameters such as ferroelectric and ferromagnetic materials, superconductors, and liquid crystals. They are formed when the symmetry of a single crystalline region is changed or reduced in the process of a phase transition, and separate regions with different orientation of the order parameter form. The response of a material to applied fields is defined by the static and dynamic properties of the domain walls. This is very important in numerous technological applications, such as nonvolatile ferromagnetic, ferroelectric memories, magnetoresistance and spin-valve devices, etc.[48]

Domain wall represents a special type of inhomogeneity. Its symmetry is lowered compared with that of the domain bulk. Large structural gradients in domain walls result in new effects that do not exist in the domain bulk.[49, 50] The detailed structure and formation energy of domain wall in conventional ferroelectrics are now well established.[51-53] On the contrary, research on the domain walls in multiferroics is scarce. Lajzerowicz predicted that domain walls in systems with two coupled order parameters could result in the emergence of one order inside the domain wall of the other.[54] For multiferroic materials, it means a net electric or magnetic moment could in principle exist in the center of domain walls while the domain themselves were

non-electric or non-magnetic. Later, Privratska and Janovec[49, 50] generalized this analysis to show what crystal symmetries might exhibit such behavior, using group-theory argument. Multiferroic $YMnO_3$ was studied and the results showed that the antiferromagnetic walls strongly interact with ferroelectric walls.[48] Research on multiferroic $GdFeO_3$ demonstrated that ferroelectric polarization and magnetization can be controlled by magnetic and electric field, respectively, which was attributed to the unique feature of composite domain walls.[55] A linear correlation between the density of ferroelastic domain walls and ferromagnetism has also been reported in thin films of $TbMnO_3$, suggesting that the ferroelastic domain walls in this antiferromagnetic material may be ferromagnetic.[56, 57] Furthermore, the converse effect of polarization emerging inside the domain walls of a magnet was demonstrated by Logginov *et al*.[58] Theoretical research has also predicted that both the domain wall thickness and the domain width of magnetoelectric multiferroics should be bigger than that of pure ferroelectrics and smaller than that of pure ferromagnets.[59] Experimental study on multiferroic $DyMnO_3$ verified this conclusion.[60] Recently, several groups reported domain wall conductivity[61] and magnetoelectricity[37, 62, 63] in BFO thin films.

Domain structure has significant effect on the properties of multiferroic BFO. It is thus very important to control the domain structure for different applications. Many factors affect the domain structure in BFO, and much research has been done on this topic. Zhang *et al*.[64] suggested that both the elastic energy and depolarization energy play important roles in determining the equilibrium domain structure in BFO. Varying film orientation and strain states leads to different results. It has been demonstrated that thicker films

favor the formation of regular domain structures.[65, 66] Chu *et al*.[67] has reported that for BFO films grown on $DyScO_3$ (DSO) with $SrRuO_3$ bottom electrode, the growth mechanism of the underlying $SrRuO_3$ layer determines the final domain structure of BFO. $SrRuO_3$ layers grown by step-flow and step-bunching mechanisms lead to domain structures with 2- and 4-polarization variants, respectively. To reduce the domain variants, a break in the degeneracy of the various polarization directions must be induced. One way to achieve this is by using vicinal substrates. Furthermore, asymmetric boundary conditions can lead to a preferred direction of the OOP component of the polarization. By carefully controlling the boundary conditions, Chu *et al*.[68] have obtained BFO films with only 71º domain walls located on (101) type planes and 109º domain walls located on (100) type planes.

1.2.3 The mechanism of photovoltaic effect in $BiFeO_3$ thin films

BFO has a narrow band gap (2.7 eV)[69] which is within the visible light range. The visible-light photovoltaic effect makes BFO a promising candidate for novel photovoltaic cells and optoelectronic devices.

In year 2003, a switchable visible-light photovoltaic effect in single domain BFO crystals was reported by Choi *et al*.[70], which triggered researchers' interests on the study of the photovoltaic effect in BFO. Normal ferroelectric photovoltaic effect in a single crystal single domain BFO is caused by the incomplete screening of polarization charge, which gives rise to the depolarization field in the sample. This depolarization field direction depends on the polarization direction, and is thus switchable.[16, 71, 72] On top of the

depolarization field, the schottky barriers at the electrode/film interface, and the different work functions of the electrodes may also induce band bending in the film, but these are independent of the polarization direction.[73]

In 2010, a very large photovoltage in BFO films with well aligned 71° domains was reported by Yang *et al*..[3] The authors proposed that the effect arises from the structurally driven electrostatic potential steps at the nanometer-scale domain walls (see figure 1.8). This new photovoltaic mechanism driven by the periodic potential steps at ferroelectric domain walls was later further explained by them in details.[74] Ferroelectric domain walls function as nanoscale generators of photovoltaic current, and the large output photovoltage is the accumulative effect of all the domain walls. They therefore proposed that photovoltaic effect should occur in any system with a similar periodic potential structure like in BFO. Actually, there is extensive literature describing anomalous ferroelectric photovoltaic effect in ceramic ferroelectrics which is explained as the result of series addition of smaller-than-band-gap photovoltages.[75-77] To sum up, when there are grains (as in polycrystals) or domains in the sample, each grain or domain generates its own photovoltaic response. The overall response of the sample is thus a set of small “batteries” in series, thus leading to large photovoltage.

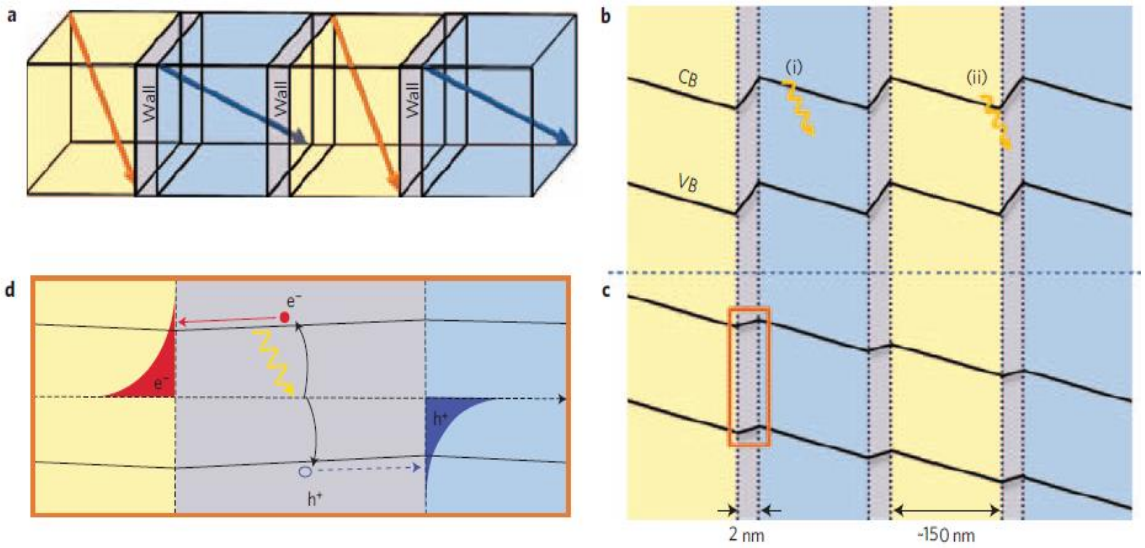

Figure 1.8 (a) Schematic of 71° domain walls (four domains with 3 domain walls). (b) Corresponding band diagram across these domains and domain walls in dark. (i) demonstrates light hitting the bulk domain and (ii) demonstrates light hitting the domain wall area. (c) Evolution of band diagram under light illumination. (d) Detailed picture of the separation of electron-hole pairs at the domain wall. Figure adapted from [3].

For the domain wall contribution, it was reported that potential steps at different domain walls are different, and the potential step at 109° domain walls is much larger than that at 71° domain walls.[61] It is thus expected that BFO films with well aligned 109º domain walls will generate a significantly larger photovoltage. However, macroscopic photovoltaic measurement of BFO films with 109º domain walls is restricted due to the presence of domains with in-plane polarizations pointing in opposite directions, thus canceling the effect. Inspired by this prediction, we therefore set our goals to study the photovoltaic effect of BFO thin films with 109º domain walls to verify the theoretical prediction of its significantly larger photovoltage. To reach our goal, we need to obtain BFO thin films with 109º domains first. We therefore started our study by controlling the domain structures in BFO films.

Since the photovoltaic response of BFO is switchable upon polarization reversal, it is possible to use the photovoltaic response as a read-out signal for ferroelectric random access memory (FeRAM). In conventional FeRAM, to read the information stored, a bias is applied to the ferroelectric capacitor, and the polarization switching current is detected. This process is destructive and a rewrite step is needed, which leads to high energy consumption and reduced device lifetime. As a result, FeRAM takes up only a negligible share of today's memory market. To solve this problem, alternative non-destructive read-out method is needed. Since the photovoltaic effect of ferroelectrics can be switchable upon polarization reversal, the coupling of the photovoltaic effect and the ferroelectric polarization can fulfill the non-destructive readout of the stored information by simply sensing the photovoltage or photocurrent. So, after studying the photovoltaic effect of BFO thin films, non-volatile memory device which is based on ferroelectric photovoltaic effect will be investigated.

1.3 Purpose of Research

The objectives of this project are:

(i) To achieve precise control of the domain structures in BFO and understand the mechanism behind it. This will be achieved by fine tuning the growth parameters of the film, such as target composition, substrate temperature etc. The domain structures will be studied using PFM and correlated to the composition and structure of the film to identify the underlying mechanism.

(ii) To study the photovoltaic effect of BFO with 109º domains. It has been suggested that the unusually large (above band gap) photovoltage observed in BFO films with 71º domains is related to the energy band bending at the domain walls.[78] Theoretical study has suggested that larger band bending should occur at 109º domain walls, leading to higher photovoltage. However, this prediction has not been tested experimentally. After achieving precise control of the domain structure in BFO, we will investigate the photovoltaic response of films with 109º domains to verify this prediction.

(iii) To explore the application of ferroelectric photovoltaic effect in non-volatile memories. Even though large photovoltage has been observed in BFO films, it is unlikely that ferroelectric materials can be used for solar energy harvesting. This is mainly due to the intrinsic high resistivity of ferroelectric materials, limiting the energy conversion efficiency. However, since the photovoltaic response of ferroelectric materials depends on the polarization direction, it can be used as the read-out signal for FeRAM. In this project, we also investigate the prototype photovoltaic effect-based FeRAM and compare it performance with other technologies under development.

Chapter 2 Control the domain structure in $BiFeO_3$ thin films

In this chapter, we present our investigation on the influence of target composition and deposition temperature on the domain structure in BFO.

2.1 Introduction to film growth and characterization techniques used

2.1.1 Pulsed laser deposition

Pulsed laser deposition (PLD) is a popular physical vapor deposition technique for functional oxide thin films.[79-81] A schematic diagram of a basic PLD system is shown in figure 2.1. The deposition chamber is equipped with target holder, substrate heater, rotators, windows, and vacuum pumps. During the deposition process, a pulsed laser beam is focused onto the target. When the laser energy density is above a threshold value, the target materials (bulk ceramics or single crystals) will be evaporated, forming a plasma plume. The plume travels normal to the target surface until it reaches the heated substrate surface, and film growth occurs. During the film deposition, the chemical environment in the chamber is controlled by various pressure gauges, and the temperature is controlled by the heating system which is connected to the substrate holder. High quality epitaxial films require laborious optimization of deposition parameters including substrate temperature, oxygen pressure, laser energy density, target-to-substrate distance etc. Moreover, different materials could have dramatically different growth windows depending on the nature of the composition elements. Our PLD system uses a KrF excimer laser with a wave length of 248 nm and a repetition rate from 1 to 20 Hz.

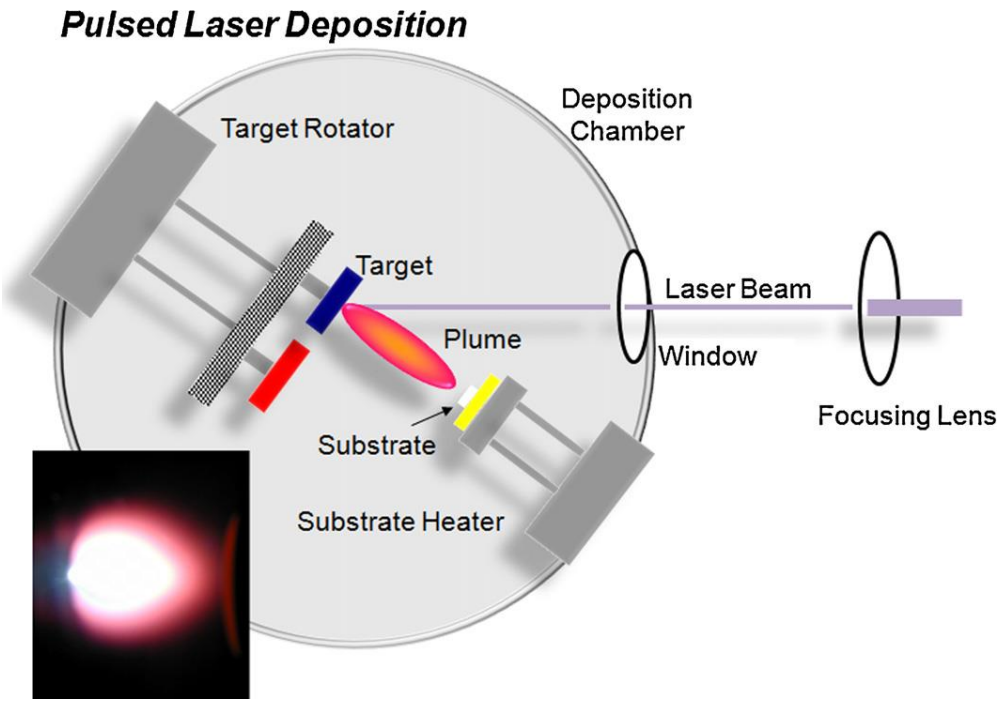

Figure 2.1 Schematic illustration of a pulsed laser deposition system. The inset shows the plume during deposition. Figure adapted from [82].

PLD technique has many advantages. The laser energy density is very high, up to 1 to 5 J/cm^2 at the target surface after focusing by the optical lens. The high energy laser ablates the target material and preserves the complex stoichiometry of target material. It is thus especially suitable for the deposition of films with complex compositions. Moreover, multiple targets in the deposition chamber enable the deposition of super-lattices, hetero-structures, and multi-layers by simply changing the targets.

The main disadvantage of PLD is that it can only grow films with very small size due to the highly forward directional property of the plume. Typically, thin films with a uniform thickness can only be obtained within a limited area, for example, 1-2 cm in diameter in our case. Therefore, PLD can only be used in the research community, but not for

industrial production. Besides this, the overheated molten particulates from the target will cause the “splashing” problem, in which case macroscopic particles will be produced.

2.1.2 Domain structure characterization by piezoelectric force microscopy

Piezoelectric force microscopy (PFM) is a variant of atomic force microscopy (AFM) which can be used to observe and manipulate ferroelectric domains at nano-scale. It is based on the converse piezoelectric effect. Since all ferroelectrics process piezoelectric property, applying an electric field to the ferroelectric sample will result in the change of its dimension. PFM is performed under contact scan mode, in which the cantilever of the AFM probe is kept in contact with the sample surface under a constant force. To reveal the polarization direction in the sample, a modulated alternative current (AC) bias $V(\omega) = V_{ac} \cos(\omega t)$ of frequency ω and amplitude V_{ac} is applied to the AFM tip. The AC bias will generate an oscillating deformation of the sample surface, $d = d_0 + D \cos(\omega t + \varphi)$, where d_0 is the equilibrium position, D is the amplitude, and φ is the phase difference with the driving field. The resulting movement of the cantilever is detected by the photodiode, through which the oscillating surface displacement is converted into an oscillating voltage. A lock-in-amplifier is then used to retrieve the amplitude (D) and phase (φ) of the sample surface deformation which is induced by converse piezoresponse effect. The amplitude signal gives information about the magnitude of the piezoelectric coefficient, while the phase signal determines the polarization direction. Figure 2.2 shows schematically working mechanism of PFM.

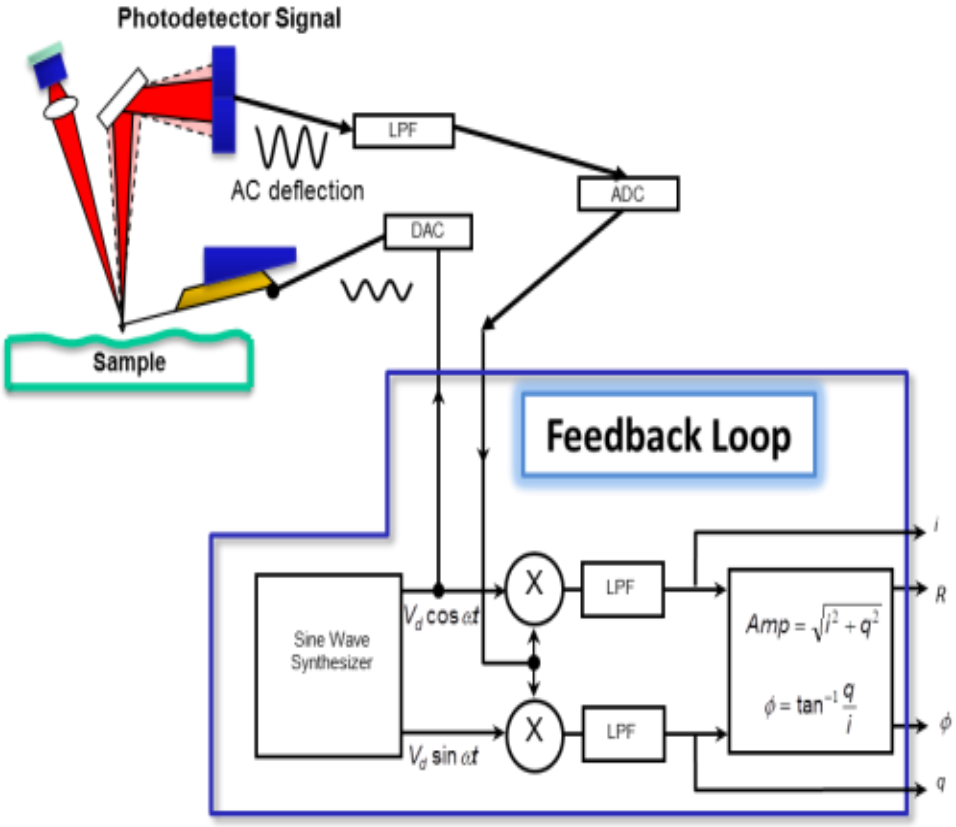

Figure 2.2 Schematic of the working mechanism of PFM.

Direction of the cantilever deflection depends on the mutual orientations of the electric field and polarization. For the upward domains (polarization vector oriented normal to the sample surface), applying a positive bias to the tip results in the shrinkage of the sample, and the sample surface oscillation is out of phase with respect to the applied AC voltage, φ = 180º. On the contrary, for downward domains, the positive bias will cause the sample to expand, and the surface oscillation is in phase with respect to the applied voltage, φ=0º. Consequently, domains with different polarization orientations will show contrasts in the PFM phase images, as shown in figure 2.3. The red line indicates the laser beam, and the panel is the photodiode which has A, B, C, D, four quadrants. Figure 2.3 (a) shows the

original state when the cantilever is undeflected, and (b) and (c) show how light spot moves when a bias is applied to the samples with oppositely oriented domains.

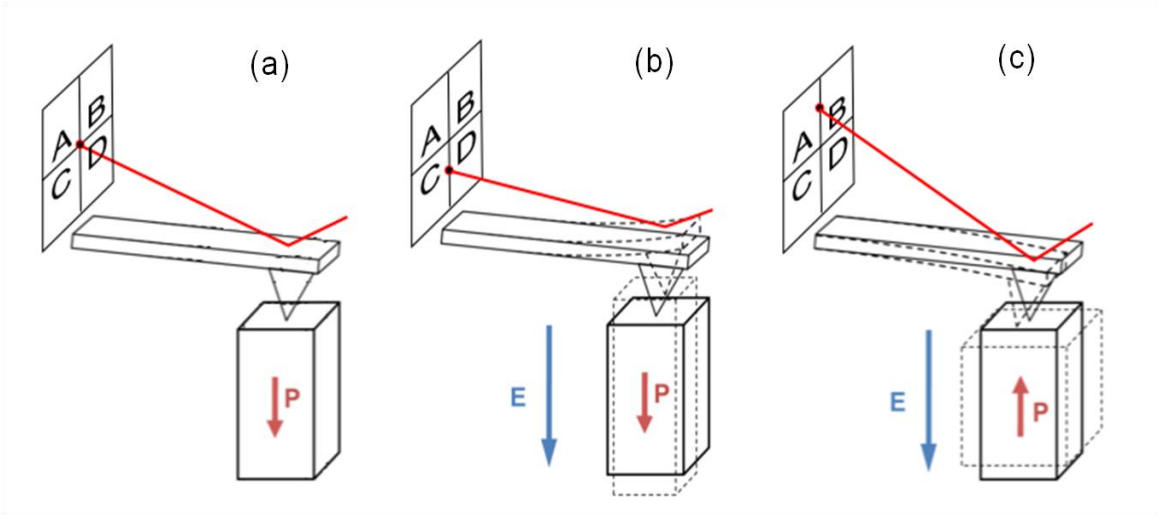

Figure 2.3 (a) The deflected laser hits the center of the photodiode when the cantilever is undeflected. (b) How the laser spot shifts when an electric field is applied to a sample with downward polarization. (c) How the laser spot shifts when the same electric field is applied to a sample with upward polarization.

Detecting the vertical deformation of the sample reveals the OOP polarization direction. This is referred to as vertical PFM. For BFO, vertical PFM alone is not enough to determine the local polarization direction since it is along the body diagonals. Later PFM detects the torsion of the cantilever caused by the lateral displacement of the sample surface. If the polarization vector is perpendicular to the electric field, a shear strain will be generated under tip bias. The shear stain leads to the angular torsion of the cantilever which can be detected by the photodiode detector.

Figure 2.3 shows schematically how the vertical and lateral deflections are detected. The photodetector is divided into four quadrants. Vertical signal = $(V_A+V_B) - (V_C+V_D)$, and lateral signal = $(V_A+V_c) - (V_b+V_D)$.

The vertical and lateral PFM give rise to OOP and in-plane (IP) domain images, respectively, through which the OOP and IP polarization component could be determined. By combining the two PFM images, three-dimensional polarization vectors can be reconstructed to reveal the exact ferroelectric domain configurations in the sample.

In the case of $(001)_{pc}$ BFO films, the contrast of PFM images can be interpreted as below. The cantilever of the AFM probe is along the $<110>_{pc}$ direction of the film, as shown in figure 2.4. The up and down components of the polarization should give rise to opposite contrast (yellow and purple, respectively, in our system) in the OOP PFM image, because their OOP piezoresponses are opposite with respect to the driving force. Domains with polarization IP components along the cantilever direction (P_2^- and P_4^- in figure 2.4 (a)) do not give rise to IP PFM signal (zero amplitude), because they bend the AFM cantilever along its length which cannot be detected by the system. A medium contrast (brown color in our system) will be generated in the IP PFM images. Domains with polarization IP component pointing to the right with respect to the cantilever direction (P_3^- in figure 2.4 (a)) should produce an opposite tone as compared with domains having polarization IP component pointing to the left (P_1^- in figure 2.4 (a)). They will generate two opposite contrasts (yellow and purple) in the PFM images, respectively. By analyzing the contrasts

of the IP and OOP PFM images, we can therefore reconstruct the domain structure in BFO thin film.

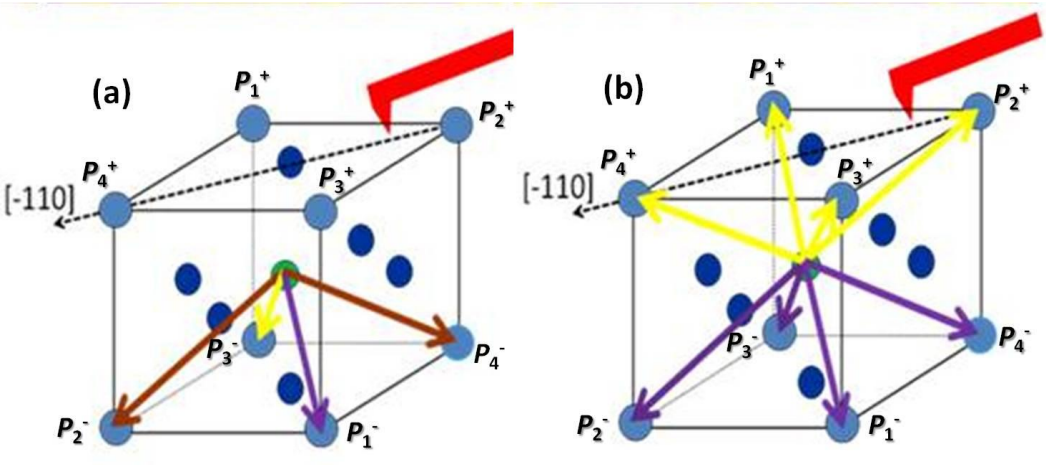

Figure 2.4 (a) The color code of IP PFM images. (b) The color code of OOP PFM images. The cantilever of the AFM probe is long the [-110] direction of the sample.

2.2 Thin film preparation and characterization procedure

Epitaxial BFO thin films are deposited on STO (001), and $GdScO_3$ $(110)_o$ (GSO, the subscript o refers to orthorhombic structure) single crystal substrates. The Structure, lattice parameter, thermal expansion coefficient of substrate and in plane misfit strains of BFO on different substrates are listed in table 2.1. Bi_xFeO_3 (B_xFO) targets (KJMT corporation) with x = 1, 0.8, 0.6, 0.5, 0.4 are used. The densities of the targets are 6.2 g/cm^3, 7.2 g/cm^3, 5.4 g/cm^3, 4.4 g/cm^3, and 4.0 g/cm^3, respectively. The difference in target density does not affect the film growth rate or growth mode under optimized condition.

Table 2.1 Structure, lattice parameter, thermal expansion coefficient of substrate and in plane misfit strains of BFO on different substrates.

Material	Structure	Lattice parameter(Å) a b c			Thermal expansion coefficient (10^{-6} K^{-1})	Misfit strain
BFO	Rhombohedral	3.965	3.965	3.965	6.5~13	/
STO	Cubic	3.905	3.905	3.905	10.4	-1.4%
GSO	Orthorhombic	5.49	5.75	7.93	10.9	0.2%

(i) Substrate and target preparation.

The substrate is ultrasonically cleaned for ten minutes in acetone and ethanol successively to remove the residuals on the surface due to polishing. The target surface should be polished with fine sand paper before deposition in order to remove the laser burned layer formed during previous deposition, which may have different composition.

(ii) Film deposition.

After cleaning, the target and substrate are placed into the deposition chamber, which will then be pumped to a base pressure of $<10^{-5}$ Torr. The target-substrate distance is ~6 cm. Then, the pumping valve is closed with a small leak left and the oxygen flow rate is adjusted to maintain a desired dynamic pressure during substrate heating. The substrate temperature is raised to desired value at a heating rate of 20 °C/min. Before the deposition, laser energy and frequency are adjusted to the desired values. KrF excimer laser with 248 nm wavelength is used in the deposition. The laser energy is around 1 J/cm^2. When the temperature of the substrate is ready, the laser is turned on and film deposition occurs. Details of the primary deposition parameters are listed in table 2.2.

Table 2.2 Deposition parameters used in this study.

Target	Substrate temperature	O_2 partial pressure	Energy density	Laser frequency	Target-substrate distance
Bi_xFeO_3, x=0.4, 0.5,0.6,0.8 and 1	680-750^o C	100mTorr	~1J/cm^2	5Hz	6 cm

(iii) Post-deposition annealing in oxygen.

When deposition is finished, the valve leak is closed and oxygen is introduced into the chamber till ambient pressure while the substrate remains at its deposition temperature. It is then cooled down to room temperature at a rate of 5 °C/min.

(iv) Characterization of thin films

The domain structures are obtained using PFM (Asylum Research MFP-3D) with Pt/Ti coated tips. JXA-8530F Field Emission Gun Electron Probe X-ray Micro-analyzer (FEG-EPMA) is used to check the film composition. X-ray diffraction (XRD) measurements are performed using a Shimadzu XRD6000 x-ray diffractometer.

2.3 Optimization of $BiFeO_3$ thin film growth parameters

During film deposition by PLD, the thermodynamic environment for the phase formation and stabilization is mainly determined by the growth temperature and oxygen pressure, which are therefore the most important growth parameters. We have mapped out the growth window for pure phase BFO thin film previously [83]. The deposition temperature and oxygen pressure can be varied from 600 ^{o}C to 750 ^{o}C, and 1 mTorr to 300 mTorr,

respectively. Lower deposition temperature and higher oxygen pressure can result in the formation of Bi_2O_3, while Fe_2O_3 will form under the opposite growth conditions.[84, 85] This phenomenon could be explained by the volatility of Bi element. During the deposition, after Bi and Fe arrive at the substrate, Bi might re-evaporate due to its volatility which is more prominent at higher temperature or lower pressure. Therefore substrate temperature and oxygen pressure can affect the re-evaporation process of Bi, and thus adjust the Bi/Fe ratio. Under proper temperature and pressure, Bi/Fe ratio will be close to 1. Similar results were also reported by Béa *et al*.[84]

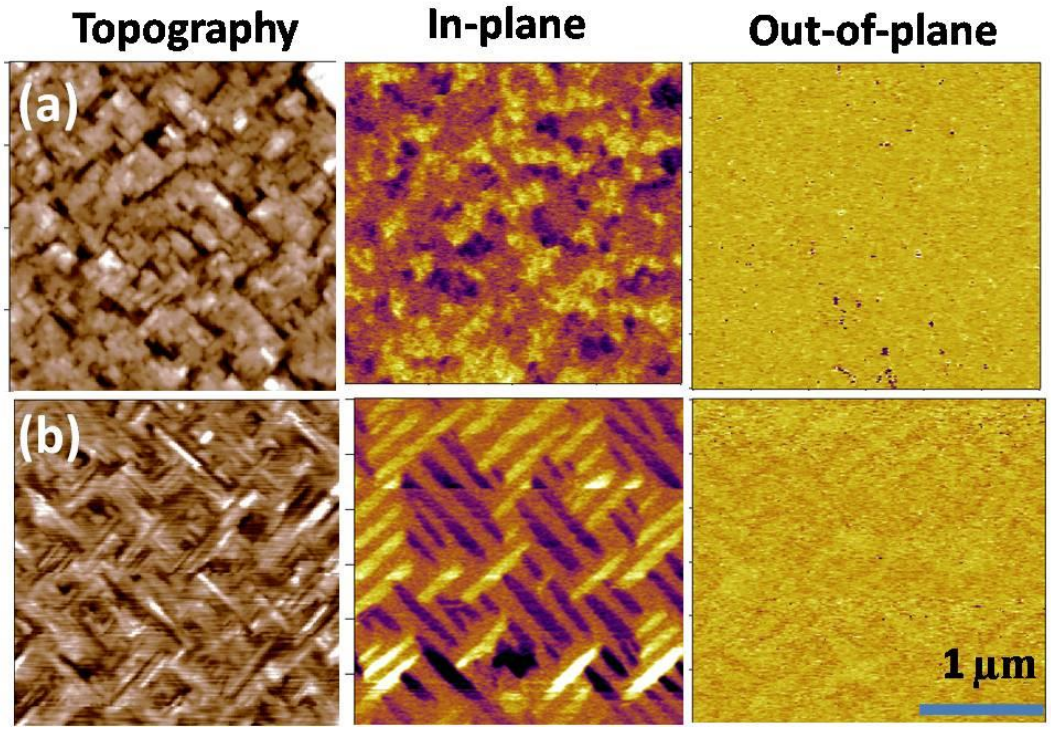

Figure 2.5 PFM images of BFO thin films on exact STO substrate grown by (a) stoichiometric BFO target and (b) $B_{0.8}$FO target.

We started our study by using a stoichiometric BFO target and (001) STO substrate. At a substrate temperature of 680 °C, the BFO films deposited using stoichiomitric target

contains a small amount of Bi_2O_3 secondary phase, and the domains are mosaic as shown in figure 2.5 (a). By reducing the Bi content in the target to 0.8, the secondary phase is eliminated and regular stripe domains are obtained as shown in figure 2.5 (b). This is contradictory to common belief that extra Bi is needed in the target to compensate its high volatility. However, we suggest that the high volatility of Bi has two competing effects: (1) more Bi being evaporated from the target than Fe during laser ablation; and (2) high possibility of Bi escaping from the substrate surface. So the film composition doesn't not depend on the target alone, and other deposition parameter such as substrate temperature is also very important.

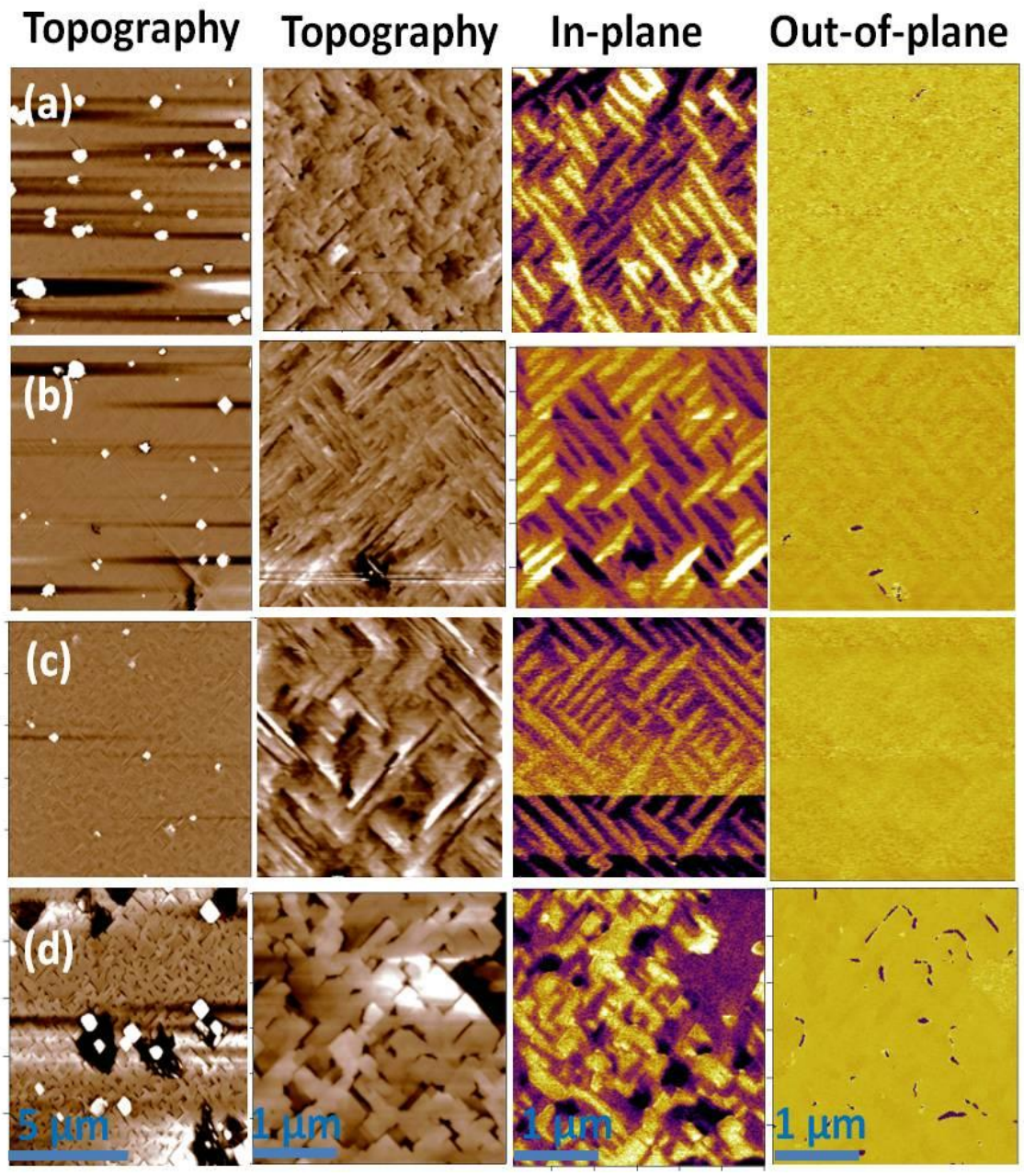

Figure 2.6 Topography and PFM images of BFO thin film grown at 680 °C, using $B_{0.8}$FO target, under oxygen pressure of (a) 300 mtorr, (b) 200 mtorr, (c) 100 mtorr, and (d) 50 mtorr.

Figure 2.6 shows the topography and PFM images of BFO thin films grown under different oxygen pressures within the deposition window. $B_{0.8}$FO target is used, and the deposition temperature is 680 °C. We can see that best quality BFO thin film with

smooth topography and regular stripes is obtained under 100 mtorr oxygen pressure. The topography becomes rougher with more particles with the increase of the oxygen pressure. On the other hand, BFO thin film starts to decompose when the oxygen pressure decreases to 50 mtorr. We can see from figure 2.6 (d) that, there are holes in the film, and the stripe domains start to disappear. We therefore fixed the oxygen pressure at 100 mtorr in this study.

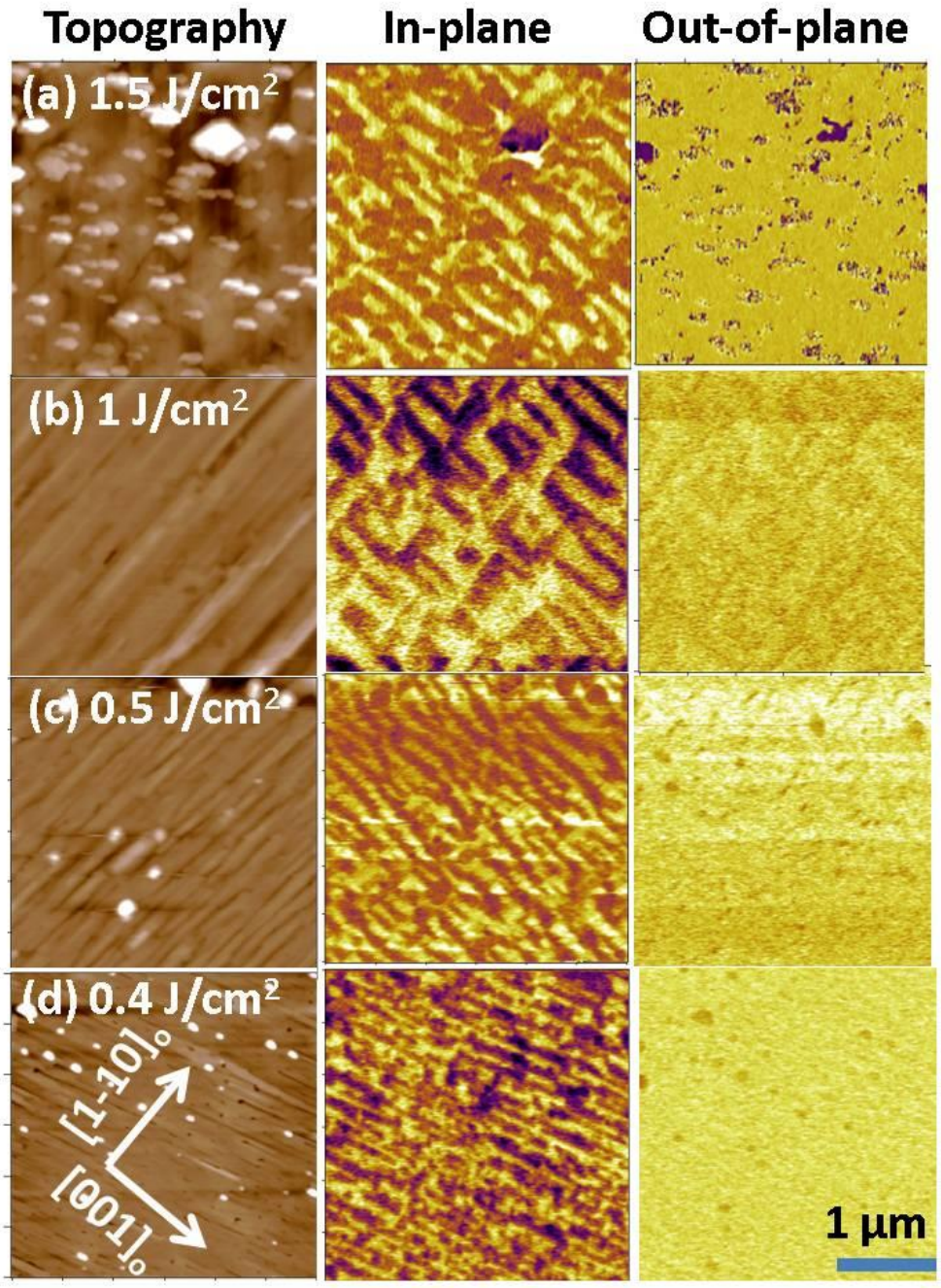

Figure 2.7 Topography and PFM images of BFO thin films on GSO substrates deposited using $B_{0.8}FO$ target at 680 °C, with the laser energy density of (a) 1.5 J/cm^2, (b) 1 J/cm^2, (c) 0.5 J/cm^2, and (d) 0.4 J/cm^2. Left: topography, Middle: IP domain image, Right: OOP domain image.

The laser energy density has been varied from 0.4 J/cm^2 to 1.5 J/cm^2. As shown in figure 2.7, for films grown using $B_{0.8}FO$ target, smooth surface and regular domains were

obtained when the laser energy density is 1.0 J/cm^2. At higher or lower energy density, particles are observed on the sample surface and the domain structure becomes random. We have fixed the laser energy density at 1 J/cm^2.

2.4 Domain structure engineering in $BiFeO_3$

2.4.1 Domain engineering through changing target composition

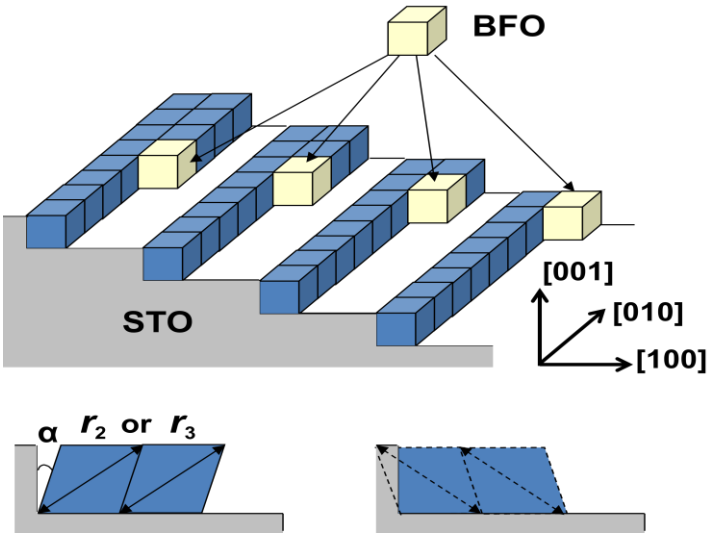

Figure 2.8 Schematic of the growth of BFO thin film on miscut STO substrate (2º miscut along [100] direction), and the structural variant selection. α is the rhombohedral distortion angle.

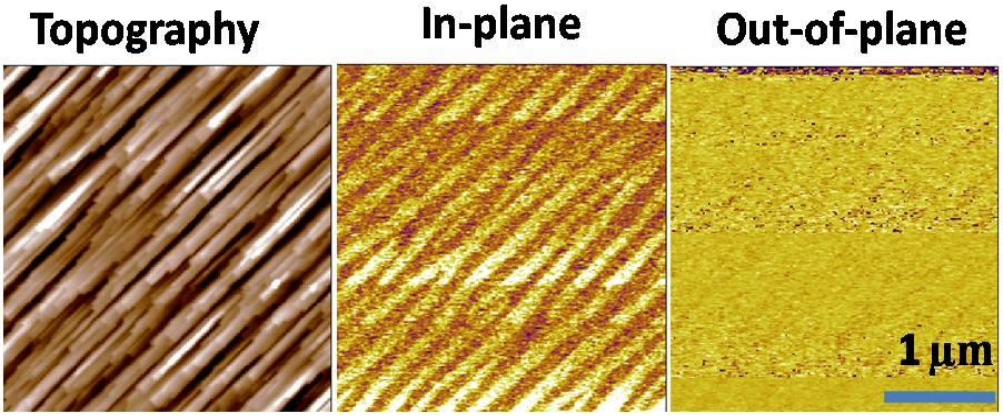

Figure 2.9 Topography, IP and OOP PFM images of BFO thin film (grown by $B_{0.8}FO$ target) on 2º miscut STO substrate.

BFO thin films grown on STO contain all 4 upward polarization variants (figure 2.5 (b)). This is expected because of the cubic symmetry of STO. A break in symmetry is necessary to reduce the polarization variants. This can be realized by using miscut (along (100) direction) substrate. The anisotropic surface states can reduce the 4 structural variants of BFO film to 2, as shown in figure 2.8. The formation of structural variant r_1 and r_4 is prohibited on miscut STO substrate, because their rhombohedral distortion is mechanically unfavorable. Indeed, the PFM images shown in figure 2.9 confirm the effect. The film topography shows a step pattern. Stripe domains with 2 structural variants separated by 71º domain walls are observed in the IP image. For films on miscut STO substrate, the stress is easier to relax along the miscut direction than along the step edges.[86] Therefore the energetically favorable distortion is along the downhill miscut direction, which results in the stripe domains with only two structural variants.

Similar effect can be achieved by using substrates with lower symmetry, such as orthorhombic DSO and GSO substrates. These substrates have a surface with non-square unit cell, resulting in anisotropic stress in pseudocubic epitaxial films. The advantage of using such substrates is that they can break the symmetry between different polarization variants, but does not introduce topographic anisotropy that may complicate the result analysis.

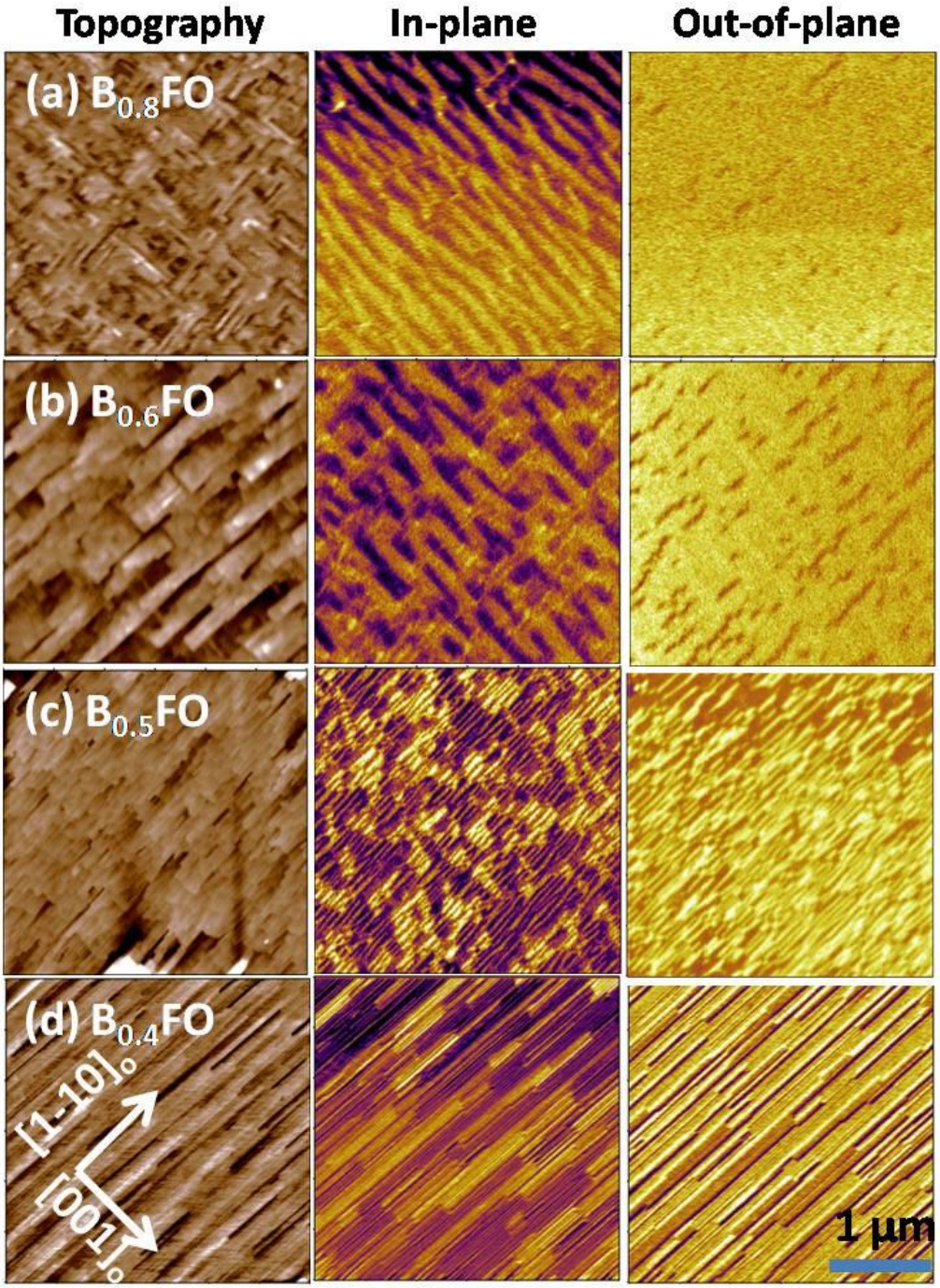

Figure 2.10 Topography and PFM images of BFO thin films on GSO substrates deposited using (a) $B_{0.8}FO$, (b) $B_{0.6}FO$, (c) $B_{0.5}FO$, and (d) $B_{0.4}FO$ targets.

Figure 2.10 shows the topography (left), IP (middle) and OOP (right) domain images of BFO films deposited at 680 ºC on GSO substrates using targets with 0.8, 0.6, 0.5 and 0.4 Bi, respectively. For the sample deposited using $B_{0.8}FO$ target, only two domain variants

are observed in the IP image, consistent with early reports on the effect of anisotropic substrates.[67, 87, 88] The OOP image shows uniform contrast, indicating that 71º domains are obtained.[28] However, since the film is deposited on GSO substrate without a bottom electrode, it is rather surprising to observe 71º domains, which are fully poled along the OOP direction. There must be an internal bias in the as-deposited films that competes with the large depolarization field. Possible origins of such internal field include (1) interface bond reconstruction,[89, 90] (2) interface valence mismatch;[91] and (3) defects, e.g. oxygen vacancies, accumulation at the interface.[92]

Interestingly, by reducing the Bi content in the target, we can change the domain structure of the as-deposited film gradually. When $B_{0.6}FO$ target is used, the domains are still mainly 71°, however, the quantity of pointing-down domains increases as shown by the increasing dark regions in the OOP domain image in figure 2.10 (b), since dark contrast in OOP PFM image means polarization pointing "down". When $B_{0.5}FO$ and $B_{0.4}FO$ targets are used, the OOP PFM images of the thin films show stripe contrast which is the characteristic of 109° domains.[93]

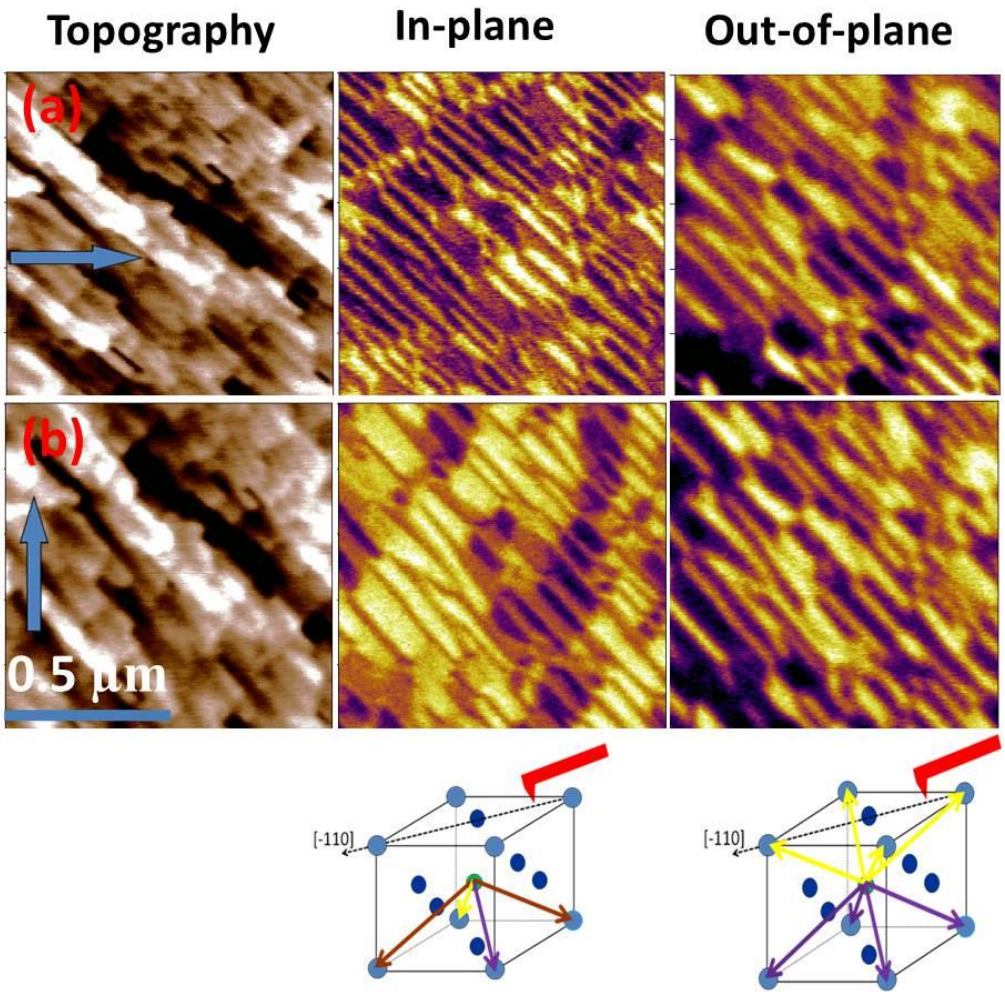

Figure 2.11 PFM images of the same area with cantilever (a) along the [1-10] direction and (b) along the [110] direction.

To confirm the exact domain variants, two sets of PFM images obtained at the same location in the film but along two orthogonal <110> directions are needed. Figure 2.11 shows such images of film grown using $B_{0.5}FO$ target. The arrows indicate the PFM cantilever orientation. For the upper set of images, the PFM cantilever is along the [1-10] direction, and for the lower set of images, the PFM cantilever is along the [110] direction. It is can be seen that the yellow-brown and purple-brown stripes in the upper IP image turn into purple-brown and yellow-brown stripes in the lower IP image, respectively. Combining both the OP and IP-PFM images, it can be confirmed that the four

polarization variants of 109º stripe domains in the film are P_1^- & P_4^+, and P_4^- & P_1^+, respectively, corresponding to two structural variants. This is consistent with the previous discussion that the anisotropic IP strain of GSO can exclude two of the structural variants. When $B_{0.5}FO$ and $B_{0.4}FO$ targets are used, the domain structure changes to 109° stripe domains completely (figure 2.10 (c, d)). The evolution from 71° to 109° domain structure indicates that the original internal bias is eliminated or balanced by another factor induced by decreasing the Bi amount in the target, and the depolarization field forces the OOP polarization to point in opposite directions. Clearly, the domain structure of BFO films is directly related to its Bi content, or rather Bi vacancies. Besides adjusting the composition of the target, another way to tune the amount of Bi in the film is by changing the substrate temperature during deposition, which will be discussed in the following section.

2.4.2 Domain engineering through adjusting deposition temperature

Due to the high volatility of Bi, increasing substrate temperature is expected to decrease the amount of Bi in the film, leading to a similar effect as decreasing Bi content in the target. We have deposited BFO films using $B_{0.8}FO$ target at substrate temperatures ranging from 680 °C to 750 °C. The results confirm our hypothesis.

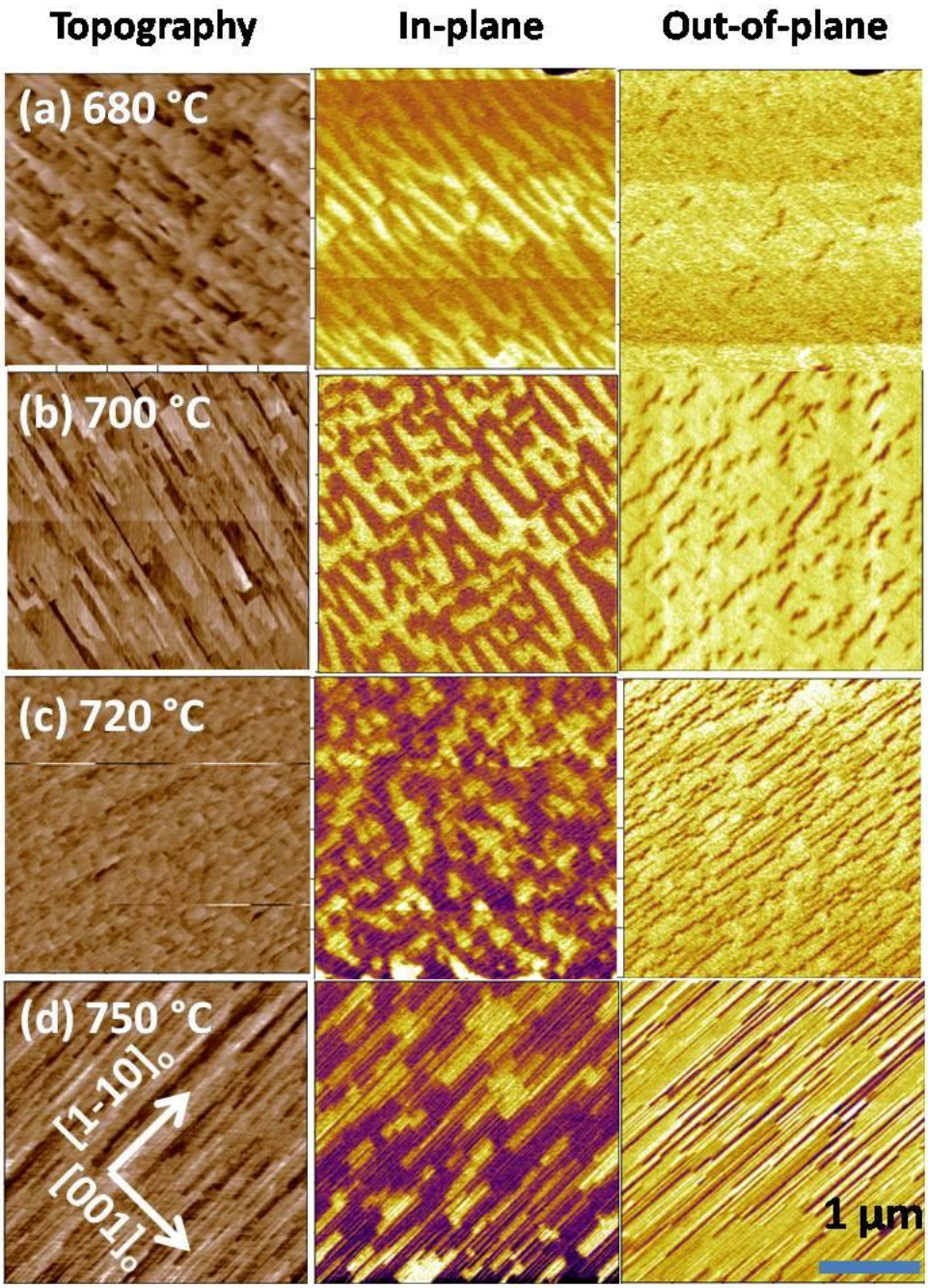

Figure 2.12 Topography and PFM images of BFO thin films on GSO substrates deposited using $B_{0.8}FO$ target at (a) 680 °C, (b) 700 °C, (c) 720 °C, and (d) 750 °C.

Figure 2.12 shows the topography (left), IP (middle) and OOP (right) PFM images of BFO films deposited at 680 ºC, 700 ºC, 720 ºC and 750 ºC, respectively. When deposited at 680 °C, the film contains only 71° stripe domains. When the temperature increases to 700 ºC, the film still contains mainly 71° domains, but the increase of the dark contrast

in the OOP PFM images indicates that the amount of 109° domains increases. At 750 °C, only 109° domains were obtained as shown in figure 2.12 (d).

2.4.3 Influence of target composition and deposition temperature on the domain structure of BFO thin films

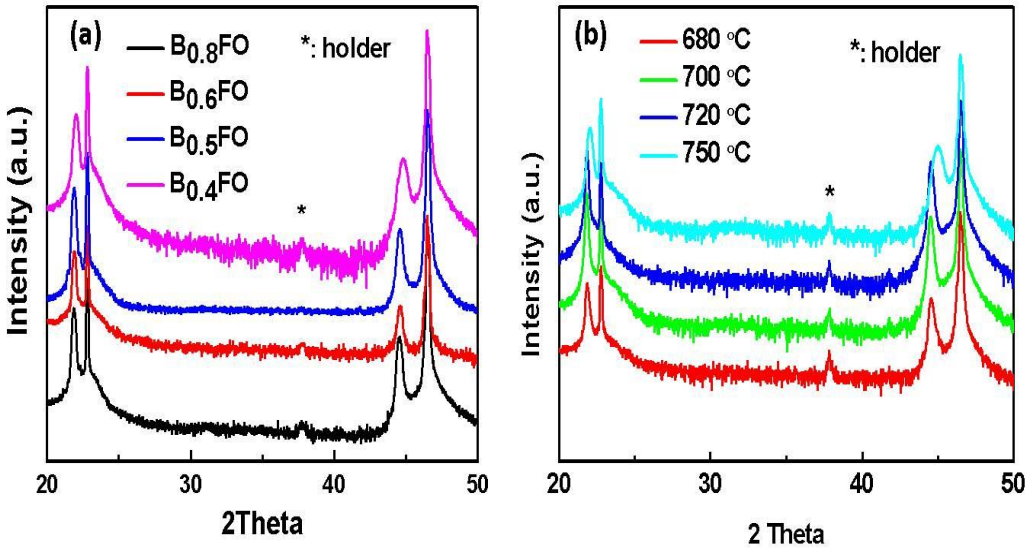

Figure 2.13 XRD patterns of films deposited (a) using targets with different composition, and (b) at different substrate temperatures.

Despite the large variation in target composition and deposition temperature used for film deposition discussed in the previous section, both sets of samples show no trace of secondary phases in the XRD patterns (figure 2.13). The questions is, what drives the change from 71 º to 109º domain structures.

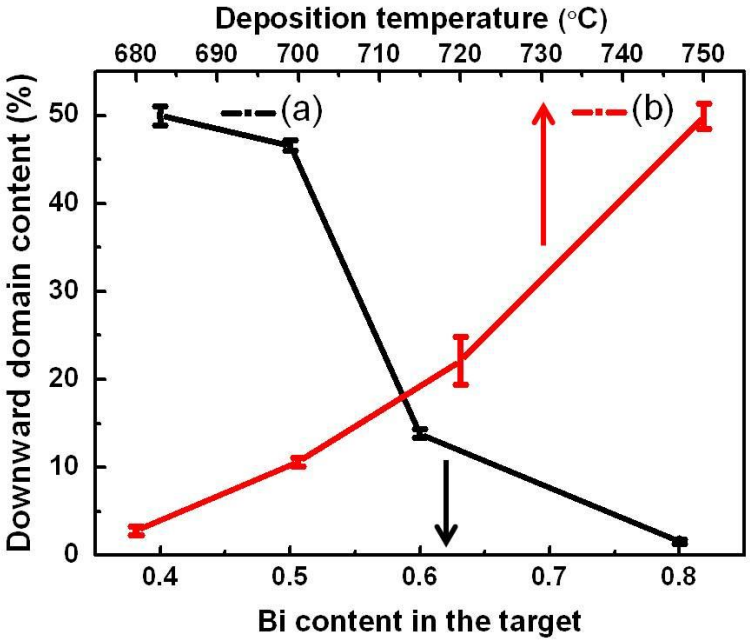

Figure 2.14 The change of the downward pointing domain regions of BFO thin film with (a) Bi content in the target and (b) deposition temperature.

The effects of target composition and substrate temperature on the domain structure of BFO film are summarized in figure 2.14 quantitatively. For both changing target and temperature experiments, five sets of samples were studied. They all show the same trend of domain evolution. For each sample, the domain structures at different locations are essentially the same. PFM images at 3 different locations were collected and analyzed quantitatively. As shown in figure 2.14, clearly, the amount of downward-pointing regions in the OOP PFM images (indicating 109° domains) increases with the decrease of Bi content in the target and the increase of the deposition temperature.[93]

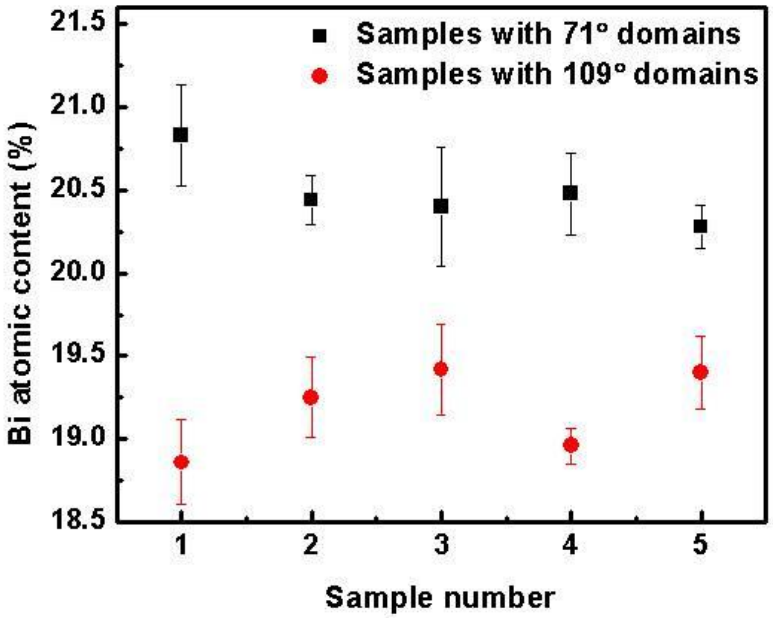

Figure 2.15 Bi content in BFO thin films with 71° and 109° domains measured using EPMA.

Both observations strongly suggest that the Bi vacancies in the films are crucial to the domain structures. To check the film composition, we conducted EPMA on five sets of 71° and 109° samples, and the results are shown in figure 2.15. The EPMA data was calibrated using a stoichiometric BFO target. The composition of the film was calculated by offline processing of raw EPMA data using GMRFilm software. We have measured 10 spots for every sample and obtained the average values. As shown in figure 2.15, Bi content in 71° samples is clearly higher than in 109° samples. The difference is three times larger than the standard deviation, confirming the reliability of the results.

Based on the EPMA results, we propose that in stoichiometric BFO films, 71° domains dominate due to the intrinsic interface effect between the film and substrate, similar to

that predicted for $KNbO_3$ film on $SrRuO_3$ coated substrate[89] or BFO film on $LaSrMnO_3$ layer[91]. We know for the fully poled upward 71° domains, a large downward depolarization field exists. This large downward depolarization field must be balanced by an upward internal bias in the as-deposited films to make the domains stable. Here, we assume the interface effects induce an upward internal bias which stabilizes the fully poled 71° domains. When using BFO target with lower Bi content or depositing the film at higher temperature, Bi vacancies will form in the thin films. We don't have means to analyze the distribution of Bi across the film thickness. However, based on the study by Matthew F. Chisholm, *et al.*, vacancies prefer to locate at the interface between the film and substrate.[47] These negatively charged Bi vacancies at the interface could generate an downward internal field that balances the interface effect, leading to 109° domains formation under depolarization field.[93]

2.5 Conclusions

We have described our effort in controlling the domain structures in BFO thin films by using BFO target with different Bi content or changing the deposition temperature. The underlying mechanism is also discussed. we conclude that:

(i) High quality epitaxial BFO thin films with different domain structures can be fabricated by tuning the target composition or the deposition temperature.

(ii) The results can be explained by a combined effect of the interface property and Bi vacancies in the films. In stoichiometric BFO films, 71° domains dominate due to

the intrinsic interface effect between the film and substrate. When using BFO target with lower Bi content or depositing the film at higher temperature, Bi vacancies in the film induce another internal field that balances the interface effect, leading to 109° domains formation under depolarization field.

Chapter 3 Photovoltaic property of $BiFeO_3$ thin films with 109° domains

Previous studies on ferroelectric photovoltaic effect mainly focused on $BaTiO_3$ and $Pb(ZrTi)O_3$, whose band gaps correspond to the UV region. BFO, a multiferroic material with robust ferroelectric and magnetic orders at room temperature[1] and a band gap within visible light range[1], provides a unique opportunity for ferroelectric photovoltaic effect study. Earlier work usually attribute the effect to the ferroelectric polarization induced depolarization field, combined with other factors, such as band offsets at the film/electrode interface[73], and defects in the thin film[94]. In 2010, Yang *et al*. reported a very large photovoltage in BFO films with well aligned 71° domains.[3] The authors proposed that the effect arises from the structurally driven electrostatic potential steps at the nanometer-scale domain walls. Another study by Seidel *et al*. has reported that the potential step at 109° domain walls is much larger than that at 71° domain walls.[61] It is thus expected that BFO films with well aligned 109° domain walls will generate a significantly larger photovoltage. However, macroscopic PV measurement of samples with 109° domain walls is prohibited due to the presence of domains with IP polarizations pointing in opposite directions (see figure 3.1 (b)), thus canceling the effect.

To investigate the photovoltaic property of BFO film with 109° domains, we tried to control the domain patterns by using miscut orthorhombic DSO substrates. We have successfully obtained BFO films with only two polarization variants forming 109° domains, leading to a net IP polarization. The net polarization direction could be switched

by an external field using a quasi-planar setup.[95] Furthermore, by combining PFM imaging with photovoltaic measurements, we have established a clear correlation between the ferroelectric domain structures of BFO and its photovoltaic property.

3.1 Experimental procedure

BFO thin films with 109° domains are epitaxially grown on exact and miscut orthorhombic DSO $(110)_o$ substrates. The lattice parameter a, b, and c of DSO are 5.44 Å, 5.71 Å, and 7.89 Å, respectively. The 2º miscut direction is along $(001)_o$ direction. $B_{0.8}FeO_3$ target is used to grow films with 109º domains. The substrate and target are prepared the same way as described previously.

The deposition oxygen pressure is 100 mtorr, and the substrate temperature is 750 ºC. Following the BFO thin film deposition, electrode patterning is carried out following standard photolithography technique. BFO film is cleaned using acetone and ethanol subsequently before the photolithography followed by drying at 110 ºC for 2 minutes. We first coat the film with a buffering layer of LOR 5A (Microchem®) using spin coater at 4000 rpm, followed by baking at 110 ºC for 2 minutes. After this, a top layer of positive photoresist EPG 510 (Everlight®) is coated at 4000 rpm, followed by baking at 110 ºC for 2 minutes again. After the spin coating, the sample is attached to a photomask for UV light (350 W) exposure for 6s using LithoPack 300 (SUSS MicroTec®). The sample is developed in TMAH (Kanto®) solution for 18 seconds to remove the exposed photoresist. 40nm thick Pt electrodes are deposited by PLD. The deposition was conducted at room temperature in vacuum (5×10^{-4} Pa), with a high laser density of 1 J/cm^2 and a frequency

of 5 Hz. After the deposition of Pt, the remaining photoresist is removed by remover solution (MicroChem®).

Polarization switching experiment is carried out using a commercial ferroelectric tester (Radiant Technologies, Inc.). For the photovoltaic measurement, current-voltage (*I-V*) curves are tested using a pA meter/DC voltage source (Hewlett Package 4140B). The light source is a Halogen lamp and the illumination energy density was 20 mW/cm^2. Each time after the polarization switching, the *I-V* curve under light is measured, and then PFM is conducted to observe the domain structure. Following this procedure, we try to establish the correlation between photovoltaic effect and domain structure.

3.2 Photovoltaic property of $BiFeO_3$ thin films with 109° domains

We use DSO $(110)_o$ single crystal as the substrates. The pseudo-cubic IP lattice constants of DSO (a=3.951, b=3.946) are close to that of BFO. Similar to GSO substrates, the asymmetric unit cell results in anisotropic stress in BFO films and a competition between multiple structural variants for strain relaxation.[67, 87] The result is that two of the structural variants are more favorable. However, even with two structural variants, the net IP polarization can still point in opposite directions (see figure 3.1 (d) and (e)). Miscut substrates are then used to generate a net IP polarization.

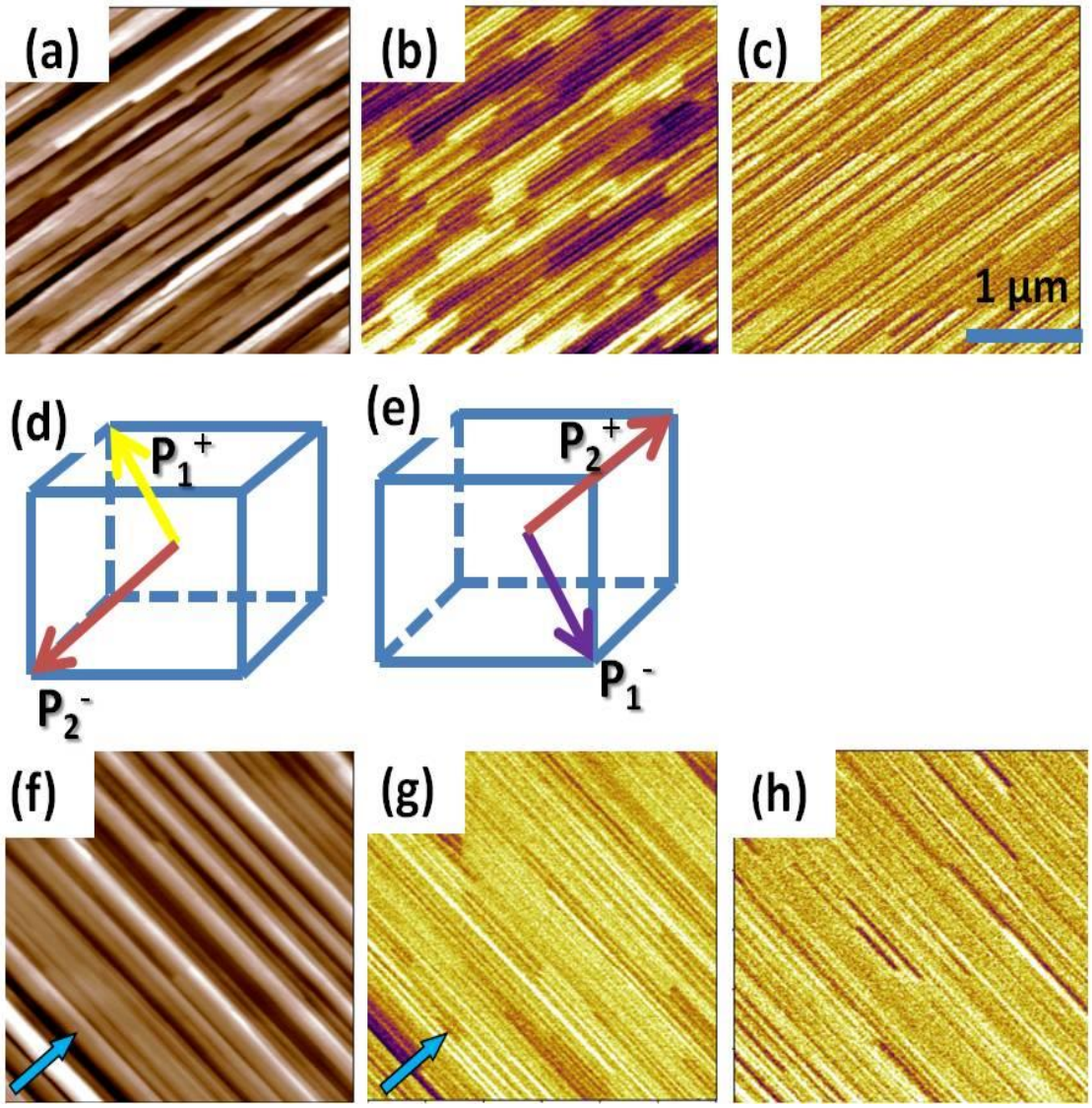

Figure 3.1 (a) Topography, (b) IP, (c) OOP PFM images of 109° BFO thin films on a normal DSO substrate. (d) and (e) Schematic of polarization variants in the sample. (f) Topography, (g) IP, and (h) OOP PFM images of 109° BFO thin films on a 2º miscut DSO substrate. The arrow in (f) shows the miscut direction, and the arrow in (g) shows the net IP polarization direction.

Figure 3.1 (a-c) shows the topography, IP and OOP PFM images of the BFO film grown on a normal DSO substrate. Combining the IP and OOP domain images, we can determine the local polarization direction as indicated in figure 3.1 (d) and (e). The bright yellow stripe corresponds to P_1^+, the two brown stripes correspond to P_2^- and P_2^+, respectively, and the dark purple stripe corresponds to P_1^-. Looking at the IP PFM image

(figure 3.1 (b)), it is clear that there are 2 structural variants with 4 polarization variants existing in this sample, and the IP polarization direction of the yellow-brown stripes is opposite to that of the purple-brown stripes. Therefore the net IP polarization and the potential steps across the 109° domain walls are cancelled, leading to negligible photovoltage across the sample. On the other hand, if we use a DSO substrate with 2º miscut towards $(001)_o$ direction (indicated by the arrow in figure 3.1 (f)), the polarization variants are reduced to 2, as shown in figure 3.1 (g, h). The IP PFM image (figure 3.1 (g)) shows only two contrasts (yellow-brown stripes), with a very small content of purple-brown stripes, while the OOP image (figure 3.1 (h)) shows bright-dark stripes. This proves that 109° domains with P_1^+ and P_2^- components dominate in this sample. This can be understood by the effect of the step edges on the substrate surface introduced by miscut.[86] When the first layer of BFO was deposited, the unit cells should start nucleating along the step edges, where the vertical interface between BFO and DSO break the IP symmetry, thus excluding 2 of 4 polarization variants. In this case, there is a net IP polarization in the sample pointing to the miscut direction, as indicated in figure 3.1 (g).

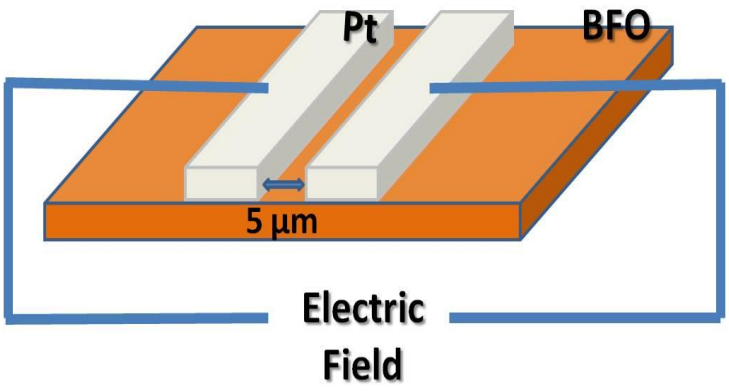

Figure 3.2 Schematic of the planar Pt electrodes on BFO thin film and the demonstration of electrical connection.

Planar electrodes are used for the measurement of photovoltaic property and the polarization switching experiment, which allows observation of domain structure evolution by PFM after polarization switching. Therefore, the correlation between the domain structure and the photovoltaic property can be established. Figure 3.2 shows the schematic of the planar device structure. Pt electrodes have a length of 500 μm, and a width of 10 μm. The distance between two electrodes (channel width) is 5 μm. Pt electrodes are parallel to the original domain stripes. When applying a voltage to the device, the electric field is perpendicular to the original domain stripes and parallel to the net IP polarization direction.[96]

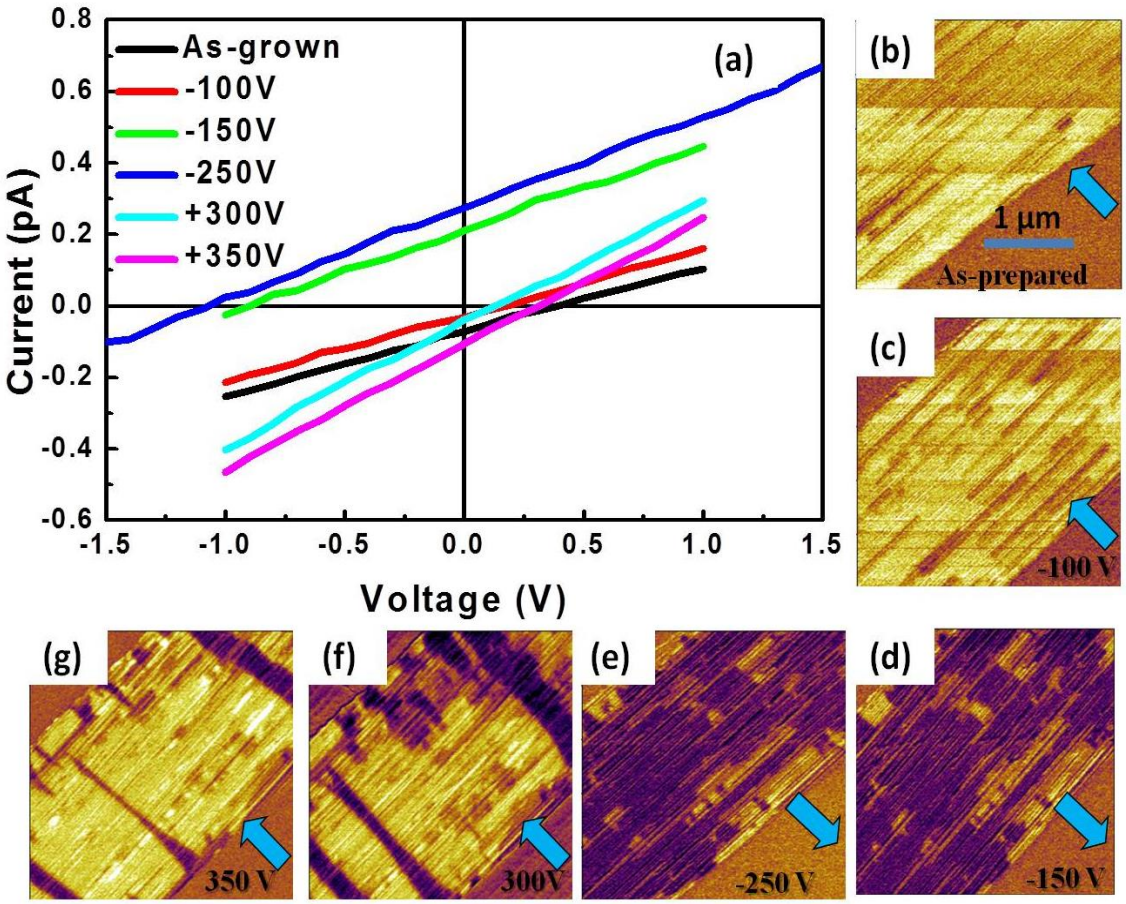

Figure 3.3 Photovoltaic property of BFO sample with mainly two polarization variants of 109° domains. (a) *I-V* curves of the as-grown sample and the sample applied by different

voltages. (b) IP PFM image of as-prepared sample. (c)-(g) IP PFM images of the sample applied by different voltages. The arrows show the net IP directions.

The *I-V* behavior of BFO films with net IP polarization is measured both in dark and under white-light illumination (energy density, 20 mW/cm^2). Under illumination, a photo induced open-circuit voltage (V_{oc}) of 0.5 V is obtained (figure 3.3 (a)), while no V_{oc} was observed in dark. To correlate the photovoltaic property with the domain structures of the film, we conducted a switching experiment. By applying an external bias to the films using the planar device, the sign of V_{oc} can be switched. At the same time, we record the IP domain images within the channel area (figure 3.3 (b-g)) (no change in OOP PFM images is observed). When a negative voltage (electric field opposite to the original net IP polarization direction) is applied to the electrodes, the original yellow-brown stripes turn into purple-brown stripes. At -150 V, almost all the yellow-brown stripes have turned into purple-brown ones (figure 3.3 (d)), indicating that the IP polarization is switched to the opposite direction (see figure 3.3 (d, e, and f)). Accompanying the switching of polarization, the V_{oc} is changed to about -1.0 V. Further increase of the voltage leads to complete switching of the polarization and the V_{oc} saturates at about -1.1 V for this device. By reversing the voltage polarity, the domain structure is switched back to its original state, and the V_{oc} returns to about 0.5 V. Note that the negative V_{oc} is larger than the corresponding positive value even after a much larger positive voltage (+350 V) is applied. This could be due to the unswitched domains as shown in figure 3.3 (f, and g). It is possible that these domains are pined by some defects in the film at the film-substrate interface. Further study is needed to clarify the actual origin of domain pinning.

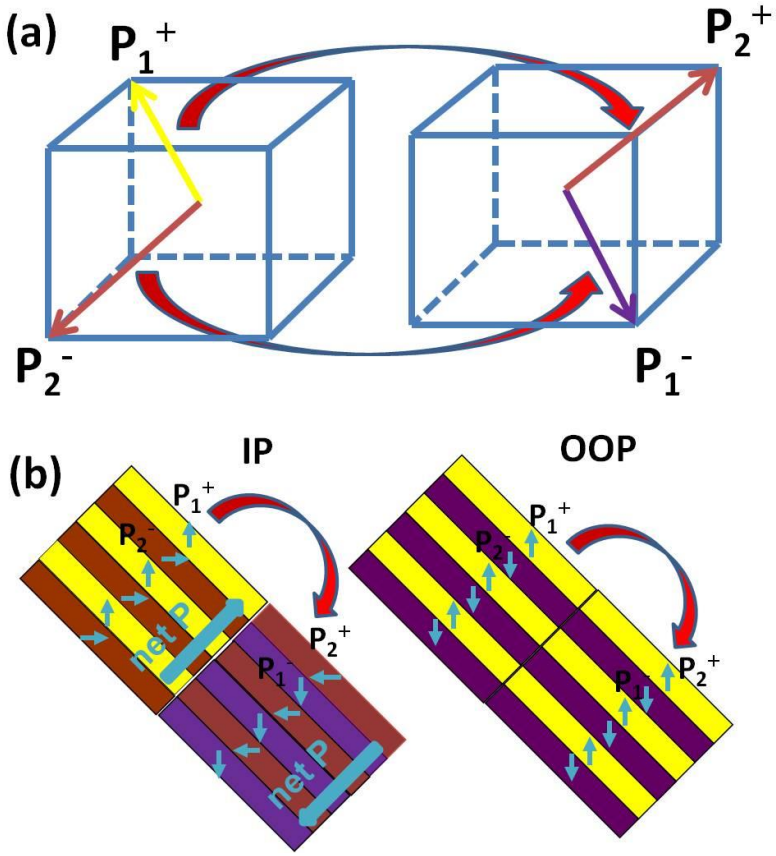

Figure 3.4 (a) Schematic of the polarization switching of 109° domains in BFO thin films. (b) Schematic of the change of IP and OOP PFM images of the 109° stripe domains after switching.

Figure 3.4 demonstrates that how polarization variants of 109º domain switch under an external voltage. The PFM images reveal that P_1^+ switches to P_2^+, while P_2^- switches to P_1^- under the negative voltage. This proves that the IP polarization reversal is achieved by 71° rotation of the individual components, while the OOP polarization component does not change during switching.

3.3 Mechanism of the photovoltaic response of $BiFeO_3$ thin films with 109° domains

The domain density of our samples is about 40 /μm. For a 5 μm channel, there are about 200 domain walls. The largest open circuit voltage we have observed in our samples is 1.6 V, which leads to a potential drop of about 8 mV/domain. This value is comparable to the microscopic measurement result reported by Yang *et al*.[3], but much smaller than the theoretically predicted 150 mV/domain. Several reasons may contribute to the lower V_{oc} observed experimentally as listed below.

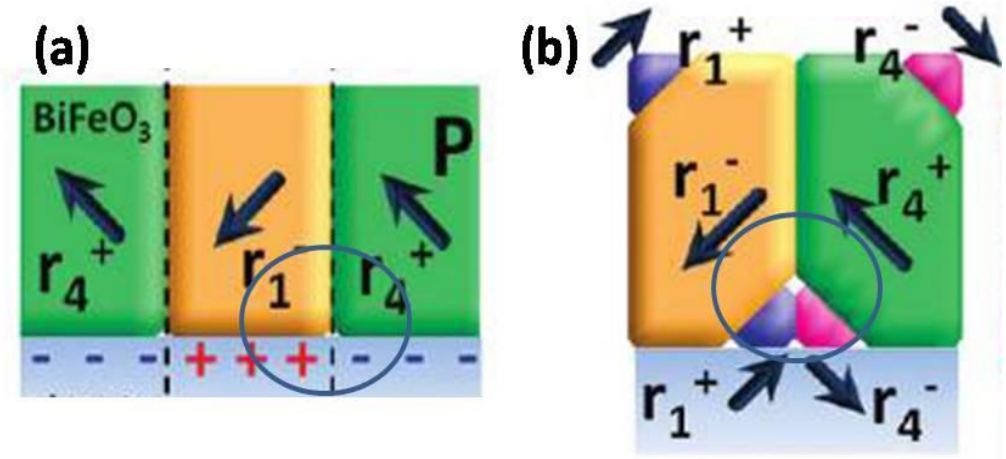

Figure 3.5 (a) Schematic of 109 domains, the circle demonstrates where the electrostatic energy is high. (b) Schematic of vortex domains. Figure captured from [97].

First, the samples with mainly two polarization variants still contain small amount of domains with opposite polarization direction. These domains will decrease the total net IP polarization, and therefore inevitably reduces the photovoltage observed. Secondly, a recent study reported that vortex domains form at the interface between BFO film with 109° domains and the substrate where the electrostatic energy is high.[97] As shown in figure 3.5 (a), the electrostatic energy at the location (circled place) between the right two 109º domains and the substrate is high, and therefore vortex domains form to reduce the

electrostatic energy. As shown in the circle of figure 3.5 (b), the IP polarization of r_1^- and r_4^+ is opposite to that of r_1^+ and r_4^-. As a consequence, the total net IP polarization decreases, which may reduce the open circuit photovoltage observed.[96]

The above two reasons cannot account for the large discrepancy between the experimentally observed photovoltage and that predicted theoretically. It is likely that the theoretical study has overestimated the effect of the domain walls, or it may not even be related. For example, residual depolarization field could also explain our results. When there is a net IP polarization, the unscreened polarization charge will generate a depolarization field which points to the opposite direction. The residual depolarization field in the film functions as the internal field which could separate electron-hole pairs that are generated by light illumination, leading to the photovoltaic effect.[96]

3.4 Conclusions

We have obtained BFO films with 109º domains and investigated their photovoltaic effect. The conclusions are:

(i) BFO domains with only 109º domains can be obtained by using miscut orthorhombic DSO substrate. The switching experiments prove that the polarization reversal of 109º domains is achieved by 71° rotation of the individual components.

(ii) Photovoltage obtained in BFO thin film with 109^{o} domain walls indicates a very small electrostatic potential step (around 8 mV) at the domain wall, which is much smaller than theoretical prediction. The results could also be explained by residual depolarization field. Therefore, the theoretical study has possibly overestimated the effect of the domain walls, or it may not even be related.

Chapter 4 Non-volatile memory based on ferroelectric photovoltaic effect

The 2010 BCC Research report on semiconductor memory estimated that the global market of memory was $46.2 billion in 2009, which will reach $79 billion in 2014. Among them, the non-volatile memory market was about $12.8 billion, reaching $25.7 billion in 2014 at a compound annual growth rate of 15%.[98] The ever-increasing demand has driven intensive research activities in this area. Currently, the non-volatile memory market is dominated by magnetic hard disk drive (HDD) and Flash memory. The HDD has a low read/write speed (>ms), which is why a dynamic random access memory (DRAM) is needed to bridge the speed gap between HDD and CPU in our computers. At present, Flash memory is widely used for portable electronics because of its low cost of production and the well-developed semiconductor fabrication technology. However, Flash memory has very low operation speed with ~10 μs programming and ~10 ms erasing time.[99] Furthermore, it can only withstand ~10^5 rewriting cycles. These drawbacks prevent it from becoming the primary storage device in personal computers. A universal memory that combines the speed of DRAM and non-volatility of Flash memory has long been the dream of electronic engineers. Several concepts are under investigation, including resistive switching random access memory (ReRAM) based on filamentary conduction and/or interface barrier modulation by defects,[100-102] phase change memory[103-105] and magnetoresistive random access memory (MRAM)[106, 107] which uses tunneling magnetoresistance effect. Although they operate at higher

speed than Flash memory, all of them have the drawback of high energy consumption which is detrimental for portable applications.

Ferroelectric random access memory (FeRAM) stores information using the spontaneous polarization of ferroelectric materials. An external voltage pulse can switch the polarization between two stable directions, representing “0” and “1”. It is non-volatile and the read/write process is very fast, which can be completed within ns. However, despite its great promise, FeRAM has a negligible share of today’s memory market. One problem is that reading in conventional FeRAM is performed by applying a bias to the ferroelectric capacitor and detecting the polarization switching current. This process is destructive and a rewrite step is needed, leading to high energy consumption and reduced device lifetime. Furthermore, it also requires a minimum capacitor size to generate enough current for the sensing circuit, leading to low memory density. To realize the full potential of FeRAM, alternative non-destructive read-out method is needed. Recently, the resistance change of a ferroelectric tunnel junction upon polarization reversal has been demonstrated and it can be used to sense the polarization direction non-destructively.[108-110] However, this approach requires the ferroelectric layer to be several nanometers thick at most, which poses a tremendous challenge on the device fabrication. Furthermore, the stability of ferroelectricity in such a thin layer and fatigue will cause reliability issues.

In this chapter, we demonstrate that the photovoltaic effect of a ferroelectric film can be used to sense the polarization direction by simply reading the open circuit photovoltage or

short circuit photocurrent, and the device has superior performance even comparable to that of DRAM. A prototype 16-cell memory based on the crossbar architecture has been prepared and tested, demonstrating the scalability of this technique.[111]

4.1 Experimental Procedure

BFO films are epitaxially grown on miscut STO (001) substrates (4º miscut towards (110) direction). $(La_{0.7},Sr_{0.3})MnO_3$ (LSMO) and Fe are used as bottom and top electrode, respectively, for the measurement of memory device. LSMO bottom electrode with the thickness of 20 nm is deposited on miscut STO substrate by PLD at 670 °C with the oxygen partial pressure of 300 mTorr. The laser energy density is fixed at 1 J/cm^2, with a frequency of 3 Hz. The growth parameters are optimized to make sure the surface roughness is low. Following the deposition of the bottom electrode, epitaxial BFO film was grown using a $B_{0.8}FO$ target with substrate temperature of 680 °C and oxygen partial pressure of 50 mTorr. The laser energy density and reparation rate were 1J/cm^2 and 10 Hz, respectively.

To prepare the top electrodes, an array of 5 μm ×5 μm squares are pattered on the BFO film surface. After the photolithography, 5 nm-thick Fe electrode is deposited followed by 5 nm Pt to protect it from oxidation. Figure 4.1 shows the sketch of the square device structure and the electrical connection. Transmittance of the Pt (5 nm)/Fe (5 nm) electrode within visible spectrum is measured using UV-Vis spectroscopy as shown in figure 4.2. About 35% of the light is transmitted, which means that the photovoltaic signals can be further improved if transparent electrodes are used.

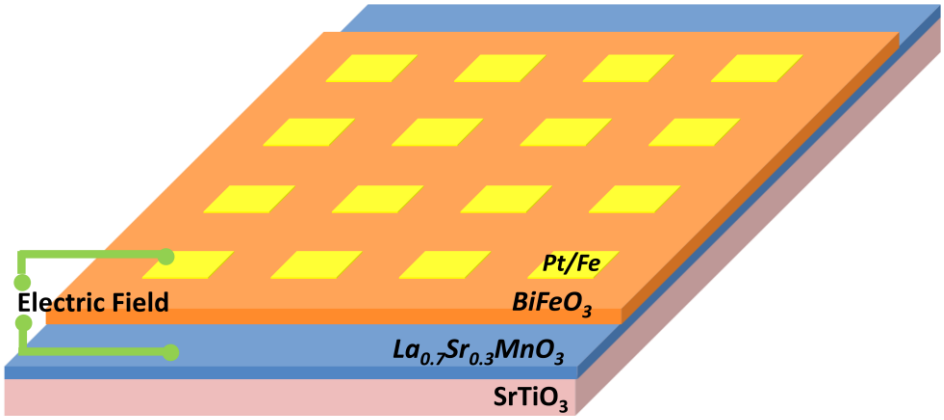

Figure 4.1 Experimental setup for the electrical characterizations of the individual capacitors. LSMO and Pt/Fe are used as the bottom and top electrodes in both cases. A four-probe micromanipulator is used to connect the device to a commercial ferroelectric tester and PicoAmp meter/DC voltage source for *P-V* and *I-V* characterizations.

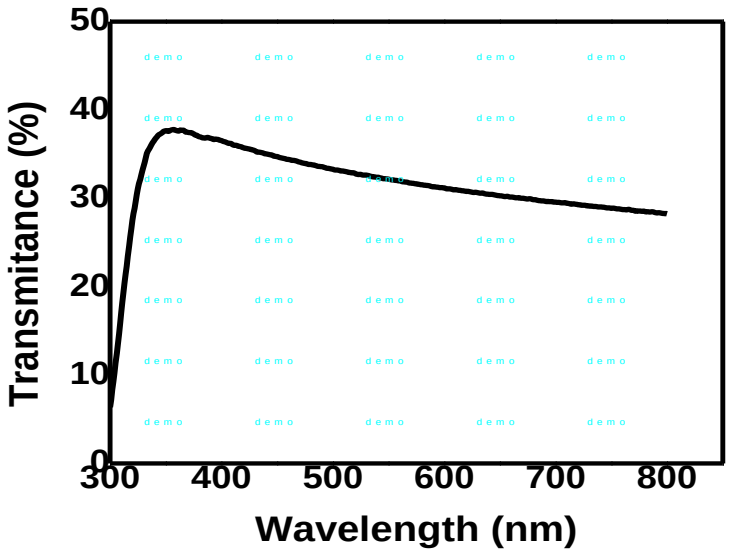

Figure 4.2 Transmittance of the Pt/Fe electrode at different wavelength measured by using UV-Vis spectroscopy.

4.2 Basic properties of single domain $BiFeO_3$

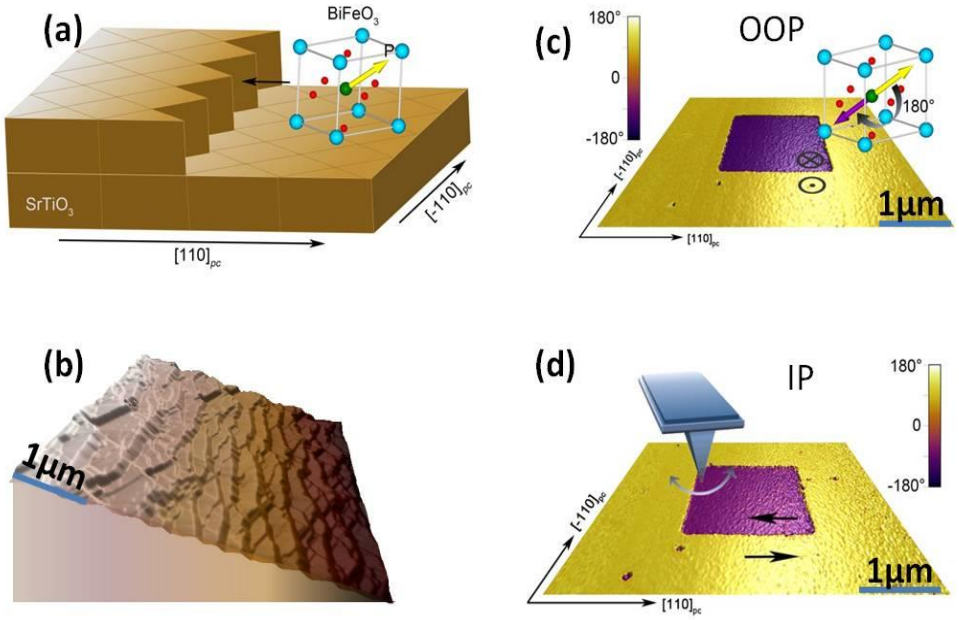

Figure 4.3 Basic properties of the STO substrate and single domain BFO films. (a) Schematic of the miscut STO substrate and corresponding BFO growth, (b) 3-D topography of the BFO film, (c) OOP PFM image of single-domain BFO film after switching the central 2 × 2 μm^2 area, the inset shows the polarization switching path, (d) corresponding IP PFM image and cantilever orientation during scan.

To eliminate complications from multiple domains in BFO, we have used miscut substrates (4° towards (110)) to obtain single domain films. Figure 4.3 (a) shows the schematic of the miscut STO substrate and corresponding BFO growth, and figure 4.3 (b) shows the 3-D topography of the BFO film. The film/substrate interface at the step edge lifts the degeneracy of the multiple domains in BFO, and the preferred polarization direction is indicated (see the yellow arrow in figure 4.3 (a)). Figure 4.3 (c) and (d) show the OOP and IP PFM domain images of the BFO film, together with the cantilever direction with respect to the film. The uniform contrasts (yellow color) of both OOP and IP PFM images confirm that the as-grown films have single domain with polarization

direction as indicated in the BFO unit cell (yellow arrow). The preferred OP polarization direction is well documented in the literature, likely a result of interface chemistry between BFO and LSMO.[91] To clarify the polarization switching path of the film, a positive DC bias of 9 V was applied to the cantilever tip during scanning over a 2 μm by 2 μm region. As a result, polarization switching occurs as shown in figure 4.3 (c) and (d). Both the OOP and IP PFM images changed to purple color. Combining the OOP and IP PFM images, it can be confirmed that the polarization switching is fulfilled by 180° rotation (see inset of figure 4.3 (c), the purple arrow shows the domain after polarization switching). Fe is chosen as the top electrode based on our investigation on the polarization fatigue in BFO. We have learned that charge injection at the electrode/BFO interface leads to domain pinning. When the pinned domains grow across the film, macroscopic fatigue occurs.[112] Furthermore, our recent study has revealed that the Schottky barrier at the interface is critical for the charge injection process. By using a low work function metal to reduce the barrier height, charge injection can be greatly reduced and fatigue performance significantly improved.[113]

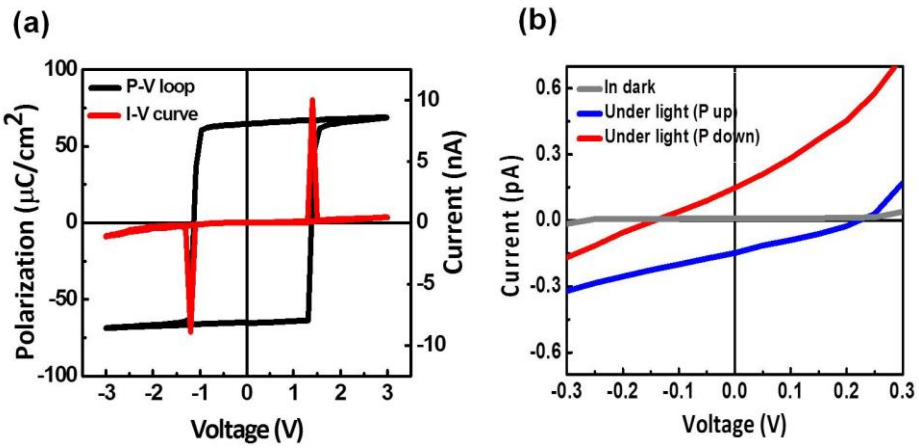

Figure 4.4 (a) typical *P-V* loop of the Fe/BFO/LSMO capacitor (red line is the corresponding *I-V* curve), and (b) *I-V* curves of the Fe/BFO/LSMO capacitor under dark and light with opposite polarization directions.

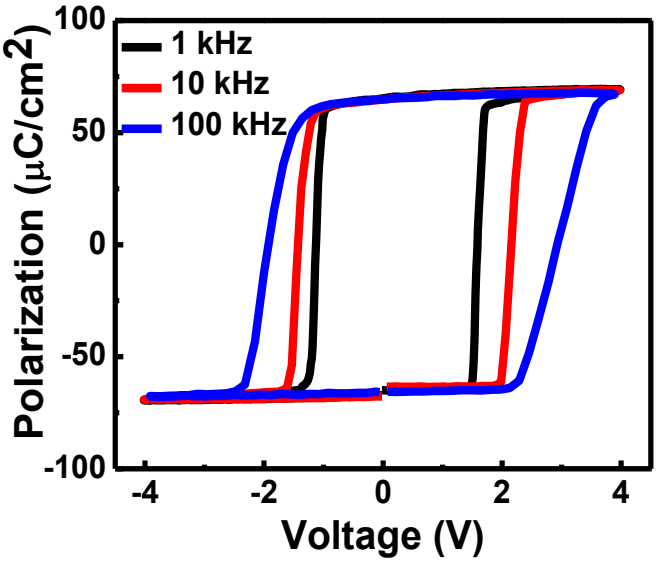

Figure 4.5 *P-V* loops measured at different frequencies.

The ferroelectric polarization-voltage (*P-V*) hysteresis loop shown in figure 4.4 (a) reveals a remnant polarization of ~ 65 μC cm^{-2} along the [001] direction, which is consistent with earlier reports.[1, 114] The red curve in figure 4.4 (a) is the relative *I-V* curve, of which the two peaks show the switching current. The square shape of the loop proves the good quality of the BFO film. The coercive voltage is quite small, about 1.3 V, which can be further reduced by decreasing the film thickness. Lower coercive voltage can reduce the energy consumption that is needed to write the memory device to ON or OFF states. The measurement frequency of the *P-V* loop is 1 kHz. The frequency dependence of the *P-V* loop is shown in figure 4.5. The ferroelectric property of the BFO films has been measured under various frequencies from 1 kHz to 100 kHz. The coercive field increases as measurement frequency increases, consistent with previous reports.[111]

For our device, the applied voltage is termed positive (negative) if a positive (negative) bias is applied to the top electrode. After poling the polarization up (down) by applying a voltage pulse of -3 V (+3 V), the *I*-*V* curves demonstrate clear photovoltaic effect under light (light source: Halogen lamp; energy density: 20 mW/cm^2). As shown in figure 4.4 (b), when polarization points upward, the I_{sc} was ~ -0.15 pA and the V_{oc} was ~ +0.22 V. After the polarization was switched, the photovoltaic effect was reversed with I_{sc} of ~ +0.16 pA and V_{oc} of ~ -0.12 V. It is thus possible to determine the polarization direction (stored information) by sensing the photovoltage or photocurrent, and this process is non-destructive. The switchable nature of the photovoltaic effect implies that it is related to the spontaneous polarization of BFO. This has been discussed in details in the literature.[16, 70, 72, 94] Basically, due to incomplete compensation of the polarization charges, the residual depolarization field is always in the opposite direction of the polarization. The depolarization field drives the photo-generated electron-hole pairs into opposite direction before they recombine. The asymmetric V_{oc} and I_{sc} under positive and negative polarization directions is likely due to the different work functions of the top and bottom electrodes, which also induces an internal field that does not depend on the polarization direction.

4.3 Properties of the Fe/$BiFeO_3$/$(La_{0.7},Sr_{0.3})MnO_3$ memory cells

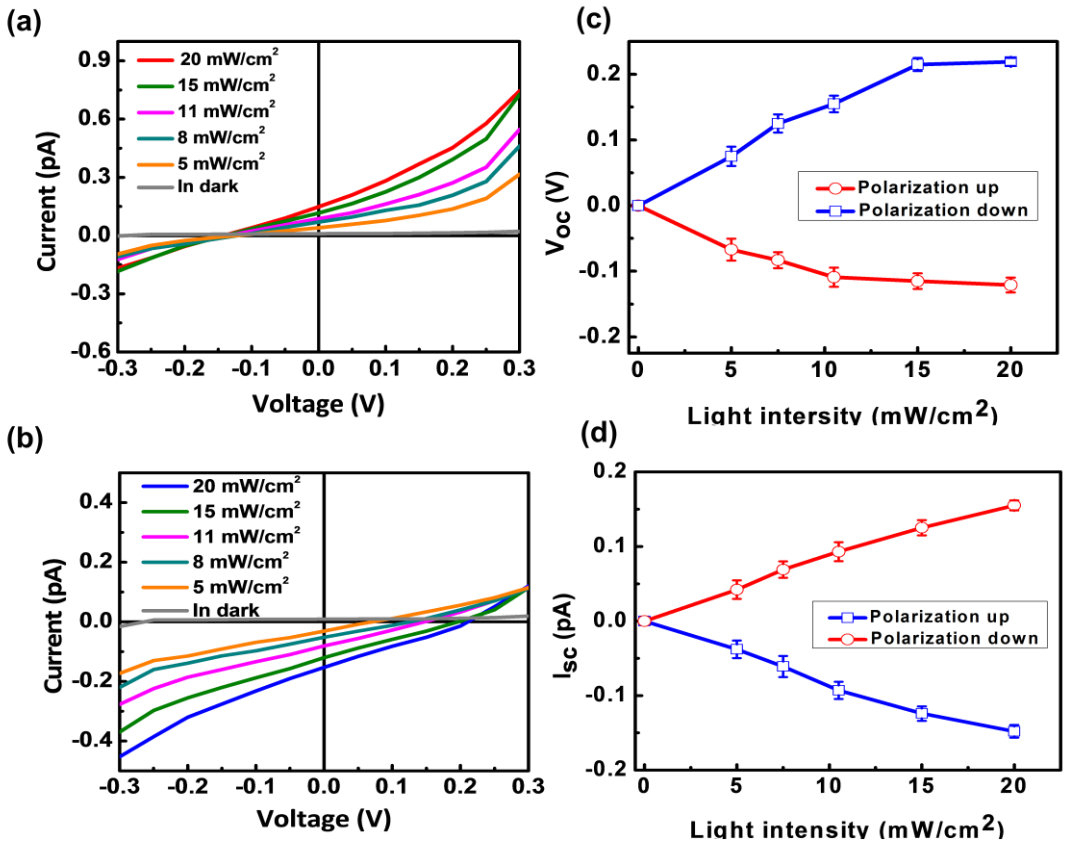

Figure 4.6 Photovoltaic property of the Fe/BFO/LSMO device. Current-voltage curves measured under different light intensity for (a) polarization down and (b) up states. (c) Open circuit voltage and (d) short circuit current as functions of light intensity for both polarization directions.

The influence of the light intensity on the photovoltaic property was tested with the light intensity increasing from 5 to 20 mW/cm^2. As expected, the photovoltaic response of the device depends on the intensity of the light. When the light intensity increases, both V_{oc} and I_{sc} increase (figure 4.6 (a-d)). The V_{oc} of the device with upward polarization saturates at ~ +0.21 V, and the V_{oc} of the device with downward polarization saturates at ~ -0.12 V. No saturation was observed for I_{sc} up to 20 mV/cm^2. The fact that the V_{oc} and I_{sc} increase with the increase of light intensity is consistent with previous report.[3] Increasing light

intensity can generate more electron-hole pairs which are separated by the internal field and lead to larger V_{oc} and I_{sc}.[3] For the measurement of V_{oc}, the circuit is open. The electrons and holes that are separated by the internal field will accumulate at the two electrodes, which will generate an electric field opposite to the internal field. When the built-in internal field is totally cancelled, photo-generated electron-hole pairs cannot be separated any longer, therefore V_{oc} saturates at this point. However, I_{sc} will not saturate with the increase of the light intensity. When measuring I_{sc}, the loop is short circuited. The separated electrons and holes will flow in the circuit,. As the light intensity increases, the fixed internal field can keep separating increasing electron-hole pairs, which thus leads to larger I_{sc}.

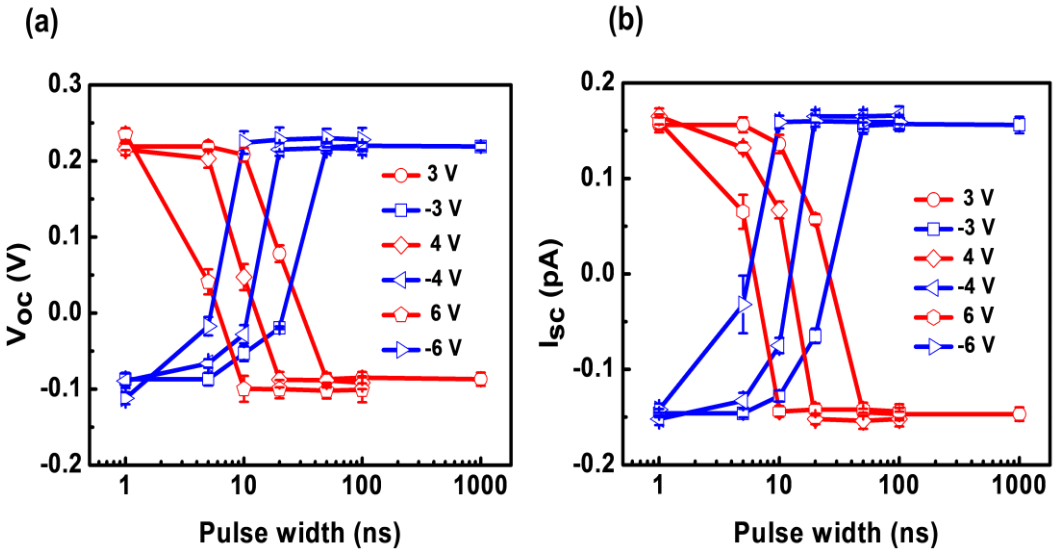

Figure 4.7 Influence of poling pulse width on (a) V_{oc}, and (b) I_{sc} of the capacitors. The switching voltage changes from ± 3 V to ± 6 V.

Operation speed is an important factor that defines the performance of memory device. To assess the operation speed of the memory cells, we measured the influence of the

poling pulse width on the photovoltaic response and the results are shown in figure 4.7. Square pulses of 1 ns to 1 ms (generated by pulse generator (Keithley 3401) are used to control the polarization direction of the film, and the *I-V* curves under 20 mW/cm^2 light are measured subsequently. When 6 V pulses are applied, the spontaneous polarization starts to switch within several ns. At 10 ns, the polarization is fully reversed and both V_{oc} and I_{sc} reach expected values. This result demonstrates that the memory cell can be written within 10 ns. However, this is by no means the limit. In fact, polarization switching by pulses of <1 ns has been reported in the literature, with the ultimate limit being set by the acoustic phonon mode (velocity of sound) in the material.[115] For the reading process, since it does not require switching of polarization and the light can be kept on whenever the device is in operation, so the photovoltaic response of every cell is always ready for reading and the speed is only limited by the RC-time constant of the circuit. What's even more attractive is that, if we use V_{oc} as the sensing signal, the memory cell can be as small as lithography technique allows since V_{oc} does not depend on the lateral size of the capacitor.

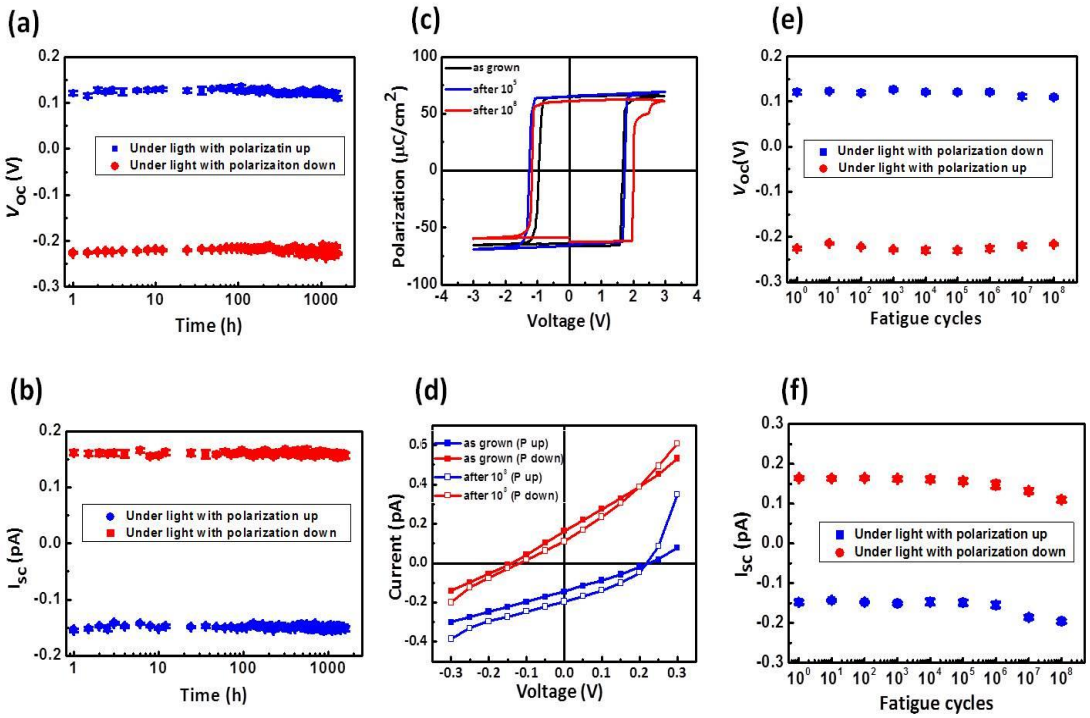

Figure 4.8 Retention and fatigue behavior of the Fe/BFO/LSMO memory cell. (a) Open circuit voltage and (b) short circuit current for both polarization directions show negligible change after 4 months. (c) Polarization-voltage loops and (d) Current-voltage curves measured after repetitive switching by pulses of ±3 V, 1 ms reveal no fatigue after 10^8 cycles. (e) Open-circuit voltage and (f) Short-circuit show slight change after the switching cycles of 10^8. In (a,b,d,e,f), blue: under light with polarization up; red: under light with polarization down.

For non-volatile memory application, long data retention and good fatigue resistance are two critical requirements. We have monitored the V_{oc} and I_{sc} of several memory cells for 4 months, no deterioration in the signal has been observed (figure 4.8 (a and b)). Furthermore, the memory cells have been subjected to bipolar switching for up to 10^8 cycles and show no sign of fatigue (figure 4.8 (c-f)). It is also well known in the ferroelectric community that fatigue can be mitigated by using oxide electrodes,

suggesting that the non-volatile memory can sustain much more read/write cycles than Flash memory.

4.4 Properties of a prototype memory device

To access the scalability of the photovoltaic effect based FeRAM, we have prepared and tested a prototype memory using the cross-bar architecture. The bottom LSMO film was patterned through photolithography process and chemical etching. After developing, LSMO electrodes with the pattern of 2000 μm × 10 μm stripes were protected by the photoresist layer. The rest of LSMO film was etched in a IBr/HCl solution of which the volume ratio of HCl to IBr is 9. Then the remaining photoresist was removed by remover. After this, the STO substrate with LSMO electrodes was cleaned by acetone and ethanol. At last, BFO film was deposited on the top of LSMO electrodes using the same deposition parameters mentioned in chapter 4.1. After the deposition of BFO film, its surface was pattered with Fe electrodes. The top stripe Fe electrodes are of the same size as the bottom LSMO electrodes but in the perpendicular direction. So a capacitor with a size of 10 × 10 μm is formed. The preparation procedure of the top Fe electrodes is same as that of the square Fe electrodes above in this chapter. After the deposition of top electrode, the remaining photoresist was removed by remover solution (MicroChem®). The schematic of the 4 × 4 cross bar device and the demonstration of the electrical connection are shown in figure 4.9.

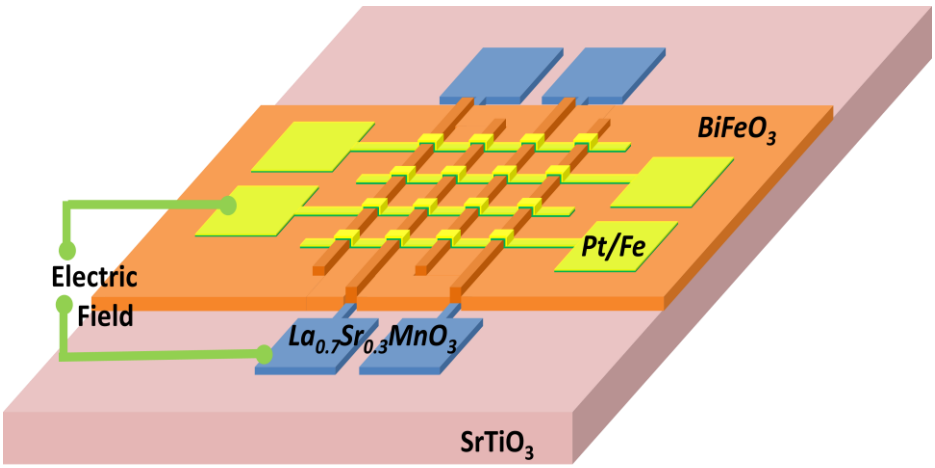

Figure 4.9 Schematic of the cross bar device structure and the demonstration of the electrical connection.

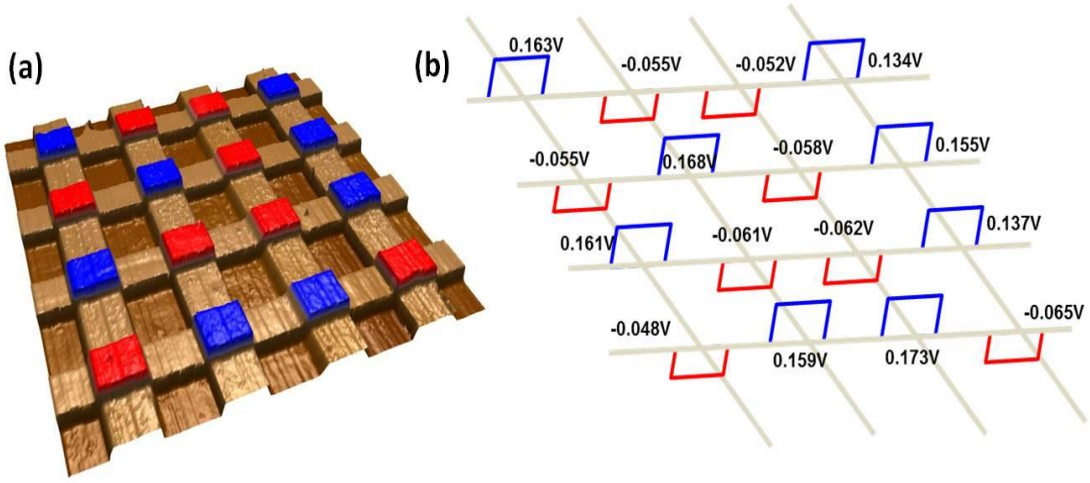

Figure 4.10 Performance of a prototype 16 cell memory based on the cross bar architecture. (a) Topography of the device with preset polarization direction indicated. Blue: polarization up, Red: polarization down. (b) Open circuit voltages of all 16 cells indicated. These are measured under 20 mW/cm^2 light. Blue: positive photovoltage, Red: negative photovoltage.

Figure 4.10 (a) depicts the topographic image of the device and each junction represents a memory cell. The 4 × 4 cross bar structure creates 16 cells in the device. In figure 4.10 (a), junctions with blue color represent memory cells with the polarization of BFO film

pointing up, while junctions with red color represent memory cells with the polarization pointing down. Despite the large size of each cell, limited by our lithography facility, all of them are fully functional. After poling the polarization direction in each cell randomly, we read the V_{oc} under 20 mW/cm^2 light by measuring the *I-V* curve of each cell. The results are shown in figure 4.10 (b). Memory cells with upward polarization show positive V_{oc} while cells with downward polarization show negative V_{oc}. The absolute values are slightly different from those obtained from the single capacitors. But the results clearly demonstrate the scalability of this concept. Typical memory performance, i.e., data retention and fatigue, has been tested for the cross bar device. The results are similar to that of the single capacitors figure 4.11.

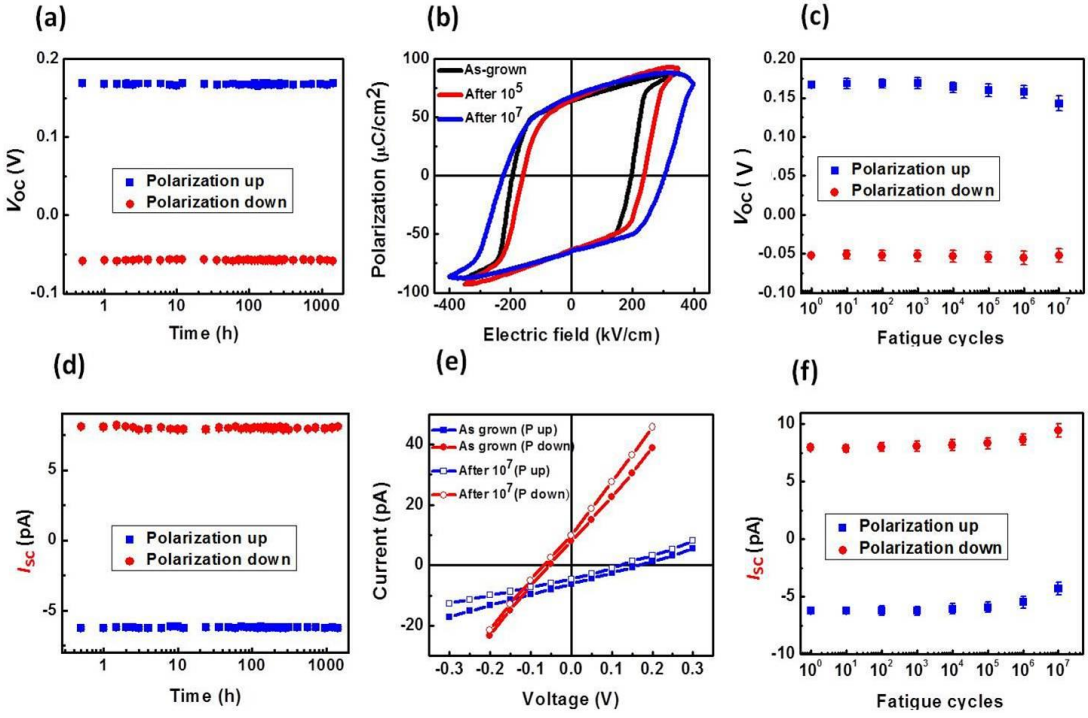

Figure 4.11 Retention and fatigue behavior of the 4 × 4 cross bar memory cell. (a) Open circuit voltage and (b) short circuit current for both polarization directions show negligible change after 2 months. (c) Polarization-Electric field loops and (d) Current-voltage curves measured after repetitive switching by pulses of ±3 V, 1 ms reveal

no fatigue after 10^7 cycles. (e) Open-circuit voltage and (f) Short-circuit current show little change after 10^7 cycles. It is also well known in the ferroelectric community that fatigue can be mitigated by using oxide electrodes, suggesting that the non-volatile memory can sustain much more read/write cycles than Flash memory. In (a,b,d,e,f), blue: under light with polarization up; red: under light with polarization down.

A fundamental problem for the cross-bar architecture is that sneak paths may form which bypass the target memory cell being addressed. Practically, this can be prevented by integrating a transistor with each cell even though it reduces the memory density. In fact, the 1 transistor 1 capacitor (1T1C) structure is employed in conventional ferroelectric memory. However, in the proposed device, each cell generates V_{oc} and I_{sc} under light by itself. No external driving force is needed during the reading process. The sneak path problem is rather different from that in the Memresistive cross bar memory. Further study is underway to clarify this issue. We also hope that this study may inspire other groups to tackle this problem as well.

Table 4.1 Comparison between different memory technologies.[108]

	Volatile Memory		Non-Volatile Memory				
	DRAM	SRAM	Flash (NAND)	MRAM magnetic	PCM phase change	FeRAM conventional	FeRAM photovoltaic
Cell element	1T1C	6T	1T	1T1C	1T1R	1T1C	1T1C
Feature size	50 nm	65 nm	90 nm	130 nm	65 nm	180 nm	50 nm #
W/E time	<10 ns	0.3 ns	0.1 ms	20 ns	50 ns	10 ns	<10 ns *
Retention	64 ms	0	>10 y	>10 y	>10 y	>10 y	>4 month* >10 y ^
Write cycles	$>10^{16}$	$>10^{16}$	$>10^{5}$	$>10^{16}$	$>10^{9}$	$>10^{14}$	$>10^{8}$ * $>10^{14}$ ^
Write voltage /energy	2.5 V 5 fJ	2.5 V 0.7 fJ	15 V 10 fJ	1.5 V 100 pJ	3 V 6 pJ	0.9-3.3 V 30 fJ	~3 V *$ 5 fJ
Read voltage	1.8 V	1 V	2 V	1.5 V	3 V	0.9-3.3 V	0 V *$

Estimated from the DRAM cell size, since the transistor size dominates if using V_{oc} as the read out signal.

* Based on current study.

^ Based on existing result on polarization retention and fatigue in the literature.

$ Since the light is on continuously during the memory operation, there is a standby power consumption. For a 1G memory with 50nm feature size and $11F^2$ fill factor, the standby power consumption is about 5.5 mW.

The non-volatile memory proposed in this paper offers several advantages over other technologies (Table 4.1). For example, the feature size is only limited by the lithography technology if photovoltage is used as the sensing signal. Compared with Flash memory, the photovoltaic FeRAM reported here has much higher operation speed and lower energy consumption. The memory density is higher than MRAM and conventional FeRAM. Writing time of less than 10 ns has been demonstrated, much faster than MRAM and Flash. The power consumption is much less than MRAM and phase change memory (PCM). Note that the results reported here are obtained from typical BFO capacitors as

proof of concept. Further optimization on the film thickness and electrode materials selection could improve the V_{oc} and I_{sc} for better performance. For example, using electrodes with larger screening length should enhance V_{oc} due to increasing depolarization field. Furthermore, the concept is not limited to BFO. Other ferroelectric materials, e.g., $Pb(ZrTi)O_3$ and $BaTiO_3$, should give rise to similar behavior. In summary, we report here a novel approach to create a non-volatile memory technology that uses the polarization dependent photovoltaic effect in ferroelectrics.[111]

4.5 Conclusions

We have investigated the properties of Fe/BFO/LSMO capacitors as possible non-volatile memory, where the stored information can be read non-destructively by sensing the photovoltaic responses. The conclusions are:

(i) Photocurrent and photovoltage with opposite signs can be obtained by controlling the polarization direction of the Fe/BFO/LSMO capacitors. Coupling the photovoltaic effect with the ferroelectric polarization allows non-destructive readout of the stored information.

(ii) The memory cells can be written within 10 ns. The reading speed is only limited by the circuit, and the read voltage is 0. Moreover, the Fe/BFO/LSMO memory cells have good data retention and fatigue resistance properties. No deterioration has been observed after four months. The memory cells have

been subjected to voltage cycling for up to 10^8 cycles and show no sign of fatigue.

(iii) The results reported here are obtained from typical BFO capacitors as proof of concept. Further optimization on the film thickness and electrode materials selection could improve the V_{oc} and I_{sc} obtained for better performance.

Chapter 5 Summary and Future Work

5.1 Summary

In this project, we have achieved precise control of the domain structures in BFO thin films by tuning the target composition and deposition temperature. The photovoltaic property of BFO thin films with regular 109° domains is studied. We conclude that the theoretical study has overestimated the energy band bending at the domain walls. Finally, we explored the possibility of using ferroelectric photovoltaic effect in non-volatile memory. The conclusions are:

(i) BFO thin films with 71° or 109° domains can be obtained by using BFO targets with different Bi content or changing the deposition temperature. Decreasing Bi content in the target or increasing the deposition temperature changes the domain structure of BFO from 71° to 109°. The results can be explained by a combined effect of the interface property and Bi vacancies in the films.

(ii) BFO thin films that contain regular 109° domains with mainly two polarization variants can be fabricated by using miscut DSO substrates. Photovoltaic effect of such films has been investigated. A direct correlation between the 109° domains switching and the photovoltaic response of the films is established, by conducting PFM study using a planar device. The photovoltage is switchable upon polarization reversal, and the IP polarization reversal of 109° domains is proven to be achieved by 71° rotation of each component. The obtained photovoltage

indicates a very small electrostatic potential step at the domain wall. It is likely that the theoretical study has overestimated the effect of the domain walls, or it may not even be related, since residual depolarization field could also explain the results.

(iii) Fe/BFO/LSMO capacitors are prepared as photovoltaic FeRAM cells since the photovoltaic responses depend on the polarization direction. It enables non-destructive read-out of the stored information (polarization direction). The memories have very high operation speed (within 10 ns), low energy consumption , and zero read voltage. Moreover, they demonstrate good data retention and fatigue resistance properties. No deterioration in the signal of V_{oc} and I_{sc} has been observed within four months, and the cells have been subjected to voltage cycling for up to 10^8 cycles and show no sign of fatigue. A prototype 4×4 cross bar devices have been prepared and tested, demonstrating the scalability of this novel technique.

5.2 Future Work

5.2.1 Enhancing the photovoltaic efficiency

Ferroelectric photovoltaic effect has potential applications in various fields. However, the efficiency is low, mainly limited by the large band gaps of ferroelectric and the small photocurrent densities.

The band gap of BFO is 2.7 eV, and its corresponding wavelength is within the visible light range (460 nm). Although it is quite small among ferroelectrics, it can still be reduced by doping. A reduced band gap could enhance the visible light absorption, and thus increase the photovoltaic efficiency. Under light illumination, the photo generates a fixed amount of electron-hole pairs. How many charges could be separated and move to the electrodes depends on how large the internal electric field is. Therefore, increasing the depolarization field could increase the V_{oc}. To achieve this, we suggest using electrodes with larger screening length. In this case, the more unscreened bound charges will generate larger depolarization field, and thus larger V_{oc}.

5.2.2 Further development of the photovoltaic FeRAM device

Despite the superior performance of photovoltaic FeRAM demonstrated in this study, there are still challenges to overcome before it can be used. One of them is the large resistance of the BFO film, which prevents a direct sensing of the photovoltage. We will explore Ca doping to reduce the internal resistance of the film while maintaining its large polarization. Another issue is the fatigue property of the device. It is well known that oxide electrodes could improve the fatigue peformance of ferroelectrics. It has been suggested that oxide electrodes can decrease the oxygen vacancy concentration at the film/electrode interface and thus reduce the domain pinning. Therefore, we will try different oxide electrodes to improve the fatigue property of the memory cells.

5.2.3 Sneak path problem in the cross bar device.

Further study will also be done on the sneak path issue which is inherent to the cross bar architecture. Different from the memresistive cross bar memory, in our proposed device, each cell at the junction generates the photovoltage or photocurrent by itself. No external deriving source is needed during the reading process. Therefore, memory cells with simple 1 × 4 and 2 × 2 crossbar structure will be fabricated to investigate whether or how each cell affects each other. For example, the property of one cell will be studied while poling three other cells to different polarizations. We can also conduct simulations to investigate the effect of parallel paths on the read-out signals.

Reference

1. Wang, J., et al., *Epitaxial $BiFeO_3$ multiferroic thin film heterostructures.* Science, 2003. **299**(5613): p. 1719-1722.
2. Ihlefeld, J.F., et al., *Optical band gap of $BiFeO_3$ grown by molecular-beam epitaxy.* Applied Physics Letters, 2008. **92**(14): p. 3.
3. Yang, S.Y., et al., *Above-bandgap voltages from ferroelectric photovoltaic devices.* Nature Nanotechnology, 2010. **5**(2): p. 143-147.
4. Seidel, J., et al., *Domain Wall Conductivity in La-Doped $BiFeO_3$.* Physical Review Letters, 2010. **105**(19): p. 197603.
5. Fridkin, V.M., *Bulk photovoltaic effect in noncentrosymmetric crystals.* Crystallography Reports, 2001. **46**(4): p. 654-658.
6. Peumans, P., S. Uchida, and S.R. Forrest, *Efficient bulk heterojunction photovoltaic cells using small-molecular-weight organic thin films.* Nature, 2003. **425**(6954): p. 158-162.
7. Chynoweth, A.G., *Surface Space-Charge Layers in Barium Titanate.* Physical Review, 1956. **102**(3): p. 705-714.
8. Kholkin, A., O. Boiarkine, and N. Setter, *Transient photocurrents in lead zirconate titanate thin films.* Applied Physics Letters, 1998. **72**(1): p. 130-132.
9. Qin, M., et al., *Stability of photovoltage and trap of light-induced charges in ferroelectric WO_3-doped $(Pb_{0.97}La_{0.03})(Zr_{0.52}Ti_{0.48})O_3$ thin films.* Applied Physics Letters, 2007. **91**(9): p. 092904.
10. Zheng, F., et al., *Separation of the Schottky barrier and polarization effects on the photocurrent of Pt sandwiched $Pb(Zr_{0.20}Ti_{0.80})O_3$ films.* Applied Physics Letters, 2008. **93**(17): p. 172101.
11. Yao, K., et al., *Large photo-induced voltage in a ferroelectric thin film with in-plane polarization.* Applied Physics Letters, 2005. **87**(21): p. 212906.
12. Qin, M., K. Yao, and Y.C. Liang, *Photovoltaic mechanisms in ferroelectric thin films with the effects of the electrodes and interfaces.* Applied Physics Letters, 2009. **95**(2): p. 022912.
13. Qin, M., et al., *Thickness effects on photoinduced current in ferroelectric $(Pb_{0.97}La_{0.03})(Zr_{0.52}Ti_{0.48})O_3$ thin films.* Journal of Applied Physics, 2007. **101**(1): p. 014104-014108.
14. Pintilie, L., et al., *Short-circuit photocurrent in epitaxial lead zirconate-titanate thin films.* Journal of Applied Physics, 2007. **101**(6): p. 064109-064109-8.
15. Yang, Y.S., et al., *Schottky barrier effects in the photocurrent of sol--gel derived lead zirconate titanate thin film capacitors.* Applied Physics Letters, 2000. **76**(6): p. 774-776.
16. Lee, D., et al., *Polarity control of carrier injection at ferroelectric/metal interfaces for electrically switchable diode and photovoltaic effects.* Physical Review B, 2011. **84**(12): p. 125305.
17. Pintilie, L., et al., *$Bi_4Ti_3O_{12}$ ferroelectric thin film ultraviolet detectors.* Applied Physics Letters, 1998. **73**(3): p. 342.
18. Shan, X.C., et al., *Fabrication of X-ray masks and applications for optical switch molding.* Sensors and Actuators A: Physical, 2003. **108**(1–3): p. 224-229.

19. Maeda, R., et al., *Piezoelectric Microactuator Devices.* Journal of Electroceramics, 2004. **12**(1-2): p. 89-100.
20. Scott, J.F. and C.A. Paz de Araujo, *Ferroelectric Memories.* Science, 1989. **246**(4936): p. 1400-1405.
21. Ichiki, M., et al., *Photovoltaic effect of lead lanthanum zirconate titanate in a layered film structure design.* Applied Physics Letters, 2004. **84**(3): p. 395-397.
22. Teague, J.R., R. Gerson, and W.J. James, *Dielectric hysteresis in single crystal $BiFeO_3$.* Solid State Communications, 1970. **8**(13): p. 1073-1074.
23. Rivera, J.P. and H. Schmid, *On the birefringence of magnetoelectric $BiFeO_3$.* Ferroelectrics, 1997. **204**(1): p. 23-33.
24. Kubel, F. and H. Schmid, *Structure of a ferroelectric and ferroelastic monodomain crystal of the perovskite BiFeO3.* Acta Crystallographica Section B, 1990. **46**(6): p. 698-702.
25. Neaton, J.B., et al., *First-principles study of spontaneous polarization in multiferroic $BiFeO_3$.* Physical Review B, 2005. **71**(1): p. 014113.
26. Zavaliche, F., et al., *Ferroelectric domain structure in epitaxial $BiFeO_3$ films.* Applied Physics Letters, 2005. **87**(18): p. 182912.
27. Li, Y.L., S.Y. Hu, and L.Q. Chen, *Ferroelectric domain morphologies of (001) $PbZr_{1-x}Ti_xO_3$ epitaxial thin films.* Journal of Applied Physics, 2005. **97**(3): p. 034112-034117.
28. Zavaliche, F., et al., *Multiferroic $BiFeO_3$ films: domain structure and polarization dynamics.* Phase Transitions, 2006. **79**(12): p. 991-1017.
29. Ederer, C. and N.A. Spaldin, *Effect of Epitaxial Strain on the Spontaneous Polarization of Thin Film Ferroelectrics.* Physical Review Letters, 2005. **95**(25): p. 257601.
30. Lebeugle, D., et al., *Very large spontaneous electric polarization in $BiFeO_3$ single crystals at room temperature and its evolution under cycling fields.* Applied Physics Letters, 2007. **91**(2): p. 022907.
31. Lebeugle, D., et al., *Room-temperature coexistence of large electric polarization and magnetic order in $BiFeO_3$ single crystals.* Physical Review B, 2007. **76**(2): p. 024116-024120.
32. Kim, D.H., et al., *Effect of epitaxial strain on ferroelectric polarization in multiferroic $BiFeO_3$ films.* Applied Physics Letters, 2008. **92**(1): p. 012911.
33. Jang, H.W., et al., *Strain-Induced Polarization Rotation in Epitaxial (001) $BiFeO_3$ Thin Films.* Physical Review Letters, 2008. **101**(10): p. 107602.
34. Chu, Y.H., et al., *Controlling magnetism with multiferroics.* Materials Today, 2007. **10**(10): p. 16-23.
35. Sosnowska, I., T. Peterlinneumaier, and E. Steichele, *Spiral magnetic-ordering in bismuth ferrite.* Journal of Physics C-Solid State Physics, 1982. **15**(23): p. 4835-4846.
36. Lebeugle, D., et al., *Electric-field-induced spin flop in $BiFeO_3$ single crystals at room temperature.* Physical Review Letters, 2008. **100**(22): p. 227602.
37. Catalan, G. and J.F. Scott, *Physics and applications of bismuth ferrite.* Advanced Materials, 2009. **21**(24): p. 2463-2485.
38. Eerenstein, W., et al., *Comment on "Epitaxial $BiFeO_3$ multiferroic thin film heterostructures".* Science, 2005. **307**(5713): p. 1203-1203.

39. Béa, H., et al., *Investigation on the origin of the magnetic moment of $BiFeO_3$ thin films by advanced x-ray characterizations.* Physical Review B, 2006. **74**(2): p. 020101.
40. Ederer, C. and N.A. Spaldin, *Weak ferromagnetism and magnetoelectric coupling in bismuth ferrite.* Physical Review B, 2005. **71**(6): p. 060401.
41. Zhao, T., et al., *Electrical control of antiferromagnetic domains in multiferroic $BiFeO_3$ films at room temperature.* Nature Materials, 2006. **5**(10): p. 823-829.
42. Chu, Y.H., et al., *Electric-field control of local ferromagnetism using a magnetoelectric multiferroic* Nature Materials, 2008. **7**(8): p. 678-678.
43. Bibes, M. and A. Barthelemy, *Multiferroics: Towards a magnetoelectric memory.* Nature Materials, 2008. **7**(6): p. 425-426.
44. Ho Won, J., et al., *Domain Engineering for Enhanced Ferroelectric Properties of Epitaxial (001) $BiFeO_3$ Thin Films.* Advanced Materials, 2009. **21**(7): p. 817-823.
45. Streiffer, S.K., et al., *Domain patterns in epitaxial rhombohedral ferroelectric films. I. Geometry and experiments.* Journal of Applied Physics, 1998. **83**(5): p. 2742-2753.
46. Wang, R.V., et al., *Reversible chemical switching of a ferroelectric film.* Physical Review Letters, 2009. **102**(4): p. 047601.
47. Chisholm, M.F., et al., *Atomic-scale compensation phenomena at polar interfaces.* Physical Review Letters, 2010. **105**(19): p. 197602.
48. Goltsev, A.V., et al., *Structure and Interaction of Antiferromagnetic Domain Walls in Hexagonal $YMnO_3$.* Physical Review Letters, 2003. **90**(17): p. 177204.
49. Přívratská, J. and V. Janovec, *Spontaneous polarization and/or magnetization in non-ferroelastic domain walls: symmetry predictions.* Ferroelectrics, 1999. **222**(1): p. 23-32.
50. Přívratská, J. and V. Janovec, *Pyromagnetic domain walls connecting antiferromagnetic non-ferroelastic magnetoelectric domains.* Ferroelectrics, 1997. **204**(1): p. 321-331.
51. Floquet, N. and C. Valot, *Ferroelectric domain walls in $BaTiO_3$: Structural wall model interpreting fingerprints in XRPD diagrams.* Ferroelectrics, 1999. **234**(1): p. 107-122.
52. Padilla, J., W. Zhong, and D. Vanderbilt, *First-principles investigation of 180° domain walls in $BaTiO_3$.* Physical Review B, 1996. **53**(10): p. R5969-R5973.
53. Meyer, B. and D. Vanderbilt, *Ab initio study of ferroelectric domain walls in $PbTiO_3$.* Physical Review B, 2002. **65**(10): p. 104111.
54. Houchmandzadeh, B., J. Lajzerowicz, and E. Salje, *Order parameter coupling and chirality of domain walls.* Journal of Physics-Condensed Matter, 1991. **3**(27): p. 5163-5169.
55. Tokunaga, Y., et al., *Composite domain walls in a multiferroic perovskite ferrite.* Nature Materials, 2009. **8**(7): p. 558-562.
56. Rubi, D., et al., *Ferromagnetism and increased ionicity in epitaxially grown $TbMnO_3$ films.* Physical Review B, 2009. **79**(10): p. 014416.
57. Venkatesan, S., et al., *Nanoscale domain evolution in thin films of multiferroic $TbMnO_3$.* Physical Review B, 2009. **80**(21).

58. Logginov, A.S., et al., *Room temperature magnetoelectric control of micromagnetic structure in iron garnet films.* Applied Physics Letters, 2008. **93**(18): p. 182510.
59. Lykah, V.A., *Domains and domain walls in multiferroic ferroelectric-ferromagnet and control of its modulation.* Ferroelectrics, 2010. **398**(1): p. 71-76.
60. Kagawa, F., et al., *Dynamics of multiferroic domain wall in spin-cycloidal ferroelectric $DyMnO_3$.* Physical Review Letters, 2009. **102**(5): p. 057604.
61. Seidel, J., et al., *Conduction at domain walls in oxide multiferroics.* Nature Materials, 2009. **8**(3): p. 229-234.
62. Lubk, A., S. Gemming, and N.A. Spaldin, *First-principles study of ferroelectric domain walls in multiferroic bismuth ferrite.* Physical Review B, 2009. **80**(10): p. 104110.
63. Daraktchiev, M., G. Catalan, and J.F. Scott, *Landau Theory of Ferroelectric Domain Walls in Magnetoelectrics.* Ferroelectrics, 2008. **375**(1): p. 122-131.
64. Zhang, J.X., et al., *Computer simulation of ferroelectric domain structures in epitaxial $BiFeO_3$ thin films.* Journal of Applied Physics, 2008. **103**(9): p. 094111.
65. Chu, Y.H., et al., *Ferroelectric size effects in multiferroic $BiFeO_3$ thin films.* Applied Physics Letters, 2007. **90**(25): p. 3.
66. Daumont, C.J.M., et al., *Tuning the atomic and domain structure of epitaxial films of multiferroic $BiFeO_3$.* Physical Review B, 2010. **81**(14): p. 144115.
67. Chu, Y.H., et al., *Nanoscale domain control in multiferroic $BiFeO_3$ thin films.* Advanced Materials, 2006. **18**(17): p. 2307.
68. Chu, Y.-H., et al., *Nanoscale Control of Domain Architectures in $BiFeO_3$ Thin Films.* Nano Letters, 2009. **9**(4): p. 1726-1730.
69. Ihlefeld, J.F., et al., *Optical band gap of $BiFeO_3$ grown by molecular-beam epitaxy.* Applied Physics Letters, 2008. **92**(14): p. 142908.
70. Choi, T., et al., *Switchable Ferroelectric Diode and Photovoltaic Effect in $BiFeO_3$.* Science, 2009. **324**(5923): p. 63-66.
71. Wei, J., Y. Kui, and C.L. Yung, *Bulk Photovoltaic Effect at Visible Wavelength in Epitaxial Ferroelectric $BiFeO_3$ Thin Films.* Advanced Materials, 2009. **22**(15): p. 1763-1766.
72. Yi, H.T., et al., *Mechanism of the switchable photovoltaic effect in ferroelectric $BiFeO_3$.* Advanced Materials, 2011. **23**(30): p. 3403-3407.
73. Yang, S.Y., et al., *Photovoltaic effects in $BiFeO_3$.* Applied Physics Letters, 2009. **95**(6): p. 062909.
74. Seidel, J., et al., *Efficient Photovoltaic Current Generation at Ferroelectric Domain Walls.* Physical Review Letters, 2011. **107**(12): p. 126805.
75. Brody, P. and F. Crowne, *Mechanism for the high voltage photovoltaic effect in ceramic ferroelectrics.* Journal of Electronic Materials, 1975. **4**(5): p. 955-971.
76. Glass, A.M., D.v.d. Linde, and T.J. Negran, *High-voltage bulk photovoltaic effect and the photorefractive process in $LiNbO_3$.* Applied Physics Letters, 1974. **25**(4): p. 233-235.
77. Brody, P., *Ferroelectric photovoltaic method and apparatus for transferring information*, U.S. Patent, Editor. 1978. p. 4103341.
78. Chiu, Y.-P., et al., *Atomic-Scale Evolution of Local Electronic Structure Across Multiferroic Domain Walls.* Advanced Materials, 2011: p. 1530-1534.

79. Lowndes, D.H., et al., *Synthesis of novel thin-film materials by pulsed laser deposition.* Science, 1996. **273**(5277): p. 898-903.
80. Christen, H.M. and G. Eres, *Recent advances in pulsed-laser deposition of complex oxides.* Journal of Physics-Condensed Matter, 2008. **20**(26): p. 264005.
81. Ashfold, M.N.R., et al., *Pulsed laser ablation and deposition of thin films.* Chemical Society Reviews, 2004. **33**(1): p. 23-31.
82. Martin, L.W., Y.H. Chu, and R. Ramesh, *Advances in the growth and characterization of magnetic, ferroelectric, and multiferroic oxide thin films.* Materials Science and Engineering: R: Reports, 2010. **68**(4-6): p. 89-133.
83. You, L., *Electrical control of ferromagnetism in multiferroic bismuth ferrite-based heterostructures*, in *School of Materials Science and Engineering*. 2011, Nanyang Technological University. p. 38.
84. Bea, H., et al., *Influence of parasitic phases on the properties of $BiFeO_3$ epitaxial thin films.* Applied Physics Letters, 2005. **87**(7): p. 072508.
85. You, L., et al., *Influence of oxygen pressure on the ferroelectric properties of epitaxial $BiFeO_3$ thin films by pulsed laser deposition.* Physical Review B (Condensed Matter and Materials Physics), 2009. **80**(2): p. 024105.
86. Sichel, R.J., et al., *Anisotropic relaxation and crystallographic tilt in $BiFeO_3$ on miscut $SrTiO_3$ (001).* Applied Physics Letters, 2010. **96**(5): p. 051901.
87. Chu, Y.H., et al., *Domain control in mulfiferroic $BiFeO_3$ through substrate vicinality.* Advanced Materials, 2007. **19**(18): p. 2662.
88. Folkman, C.M., et al., *Stripe domain structure in epitaxial (001) $BiFeO_3$ thin films on orthorhombic $TbScO_3$ substrate.* Applied Physics Letters, 2009. **94**(25): p. 251911.
89. Duan, C.G., et al., *Interface effect on ferroelectricity at the nanoscale.* Nano Letters, 2006. **6**(3): p. 483-487.
90. Singh-Bhalla, G., et al., *Built-in and induced polarization across $LaAlO_3/SrTiO_3$ heterojunctions.* Nature Physics, 2011. **7**(1): p. 80-86.
91. Yu, P., et al., *Interface control of bulk ferroelectric polarization.* Proceedings of the National Academy of Sciences of the United States of America, 2012.**109**(25): p.9710.
92. Yuan, G.L., et al., *The dependence of oxygen vacancy distributions in $BiFeO_3$ films on oxygen pressure and substrate.* Applied Physics Letters, 2009. **95**(1): p. 012904.
93. Guo, R., et al., *Influence of target composition and deposition temperature on the domain structure of $BiFeO_3$ thin films.* AIP Advances. **2**(4): p. 042104-7.
94. Ji, W., K. Yao, and Y.C. Liang, *Bulk photovoltaic effect at visible wavelength in epitaxial ferroelectric $BiFeO_3$ thin films.* Advanced Materials, 2010. **22**(15): p. 1763-1766.
95. You, L., et al., *Polarization switching in quasiplanar $BiFeO_3$ capacitors.* Applied Physics Letters, 2010. **97**(6): p.062910-1.
96. Guo, R., et al., *Photovoltaic property of $BiFeO_3$ thin films with 109 degrees domains.* Applied Physics Letters, 2011. **99**(12): p.122902-1.
97. Nelson, C.T., et al., *Spontaneous Vortex Nanodomain Arrays at Ferroelectric Heterointerfaces.* Nano Letters, 2011. **11**(2): p. 828-834.
98. *Semiconductor memory: technologies and global markets*. 2010.

99. Sun Il, S., et al., *SONOS-type flash memory cell with metal/Al_2O_3/SiN/Si_3N_4/Si structure for low-voltage high-speed program/erase operation* IEEE Electron Device Letters, 2008. **29**(5): p. 512-514.
100. Yang, J.J., et al., *Memristive switching mechanism for metal/oxide/metal nanodevices.* Nature Nanotechnology, 2008. **3**(7): p. 429-433.
101. Waser, R. and M. Aono, *Nanoionics-based resistive switching memories.* Nature Materials, 2007. **6**(11): p. 833-840.
102. Kwon, D.H., et al., *Atomic structure of conducting nanofilaments in TiO_2 resistive switching memory.* Nature Nanotechnology, 2010. **5**(2): p. 148-153.
103. Wuttig, M. and N. Yamada, *Phase-change materials for rewriteable data storage.* Nature Materials, 2007. **6**(11): p. 824-832.
104. Kolobov, A.V., et al., *Understanding the phase-change mechanism of rewritable optical media.* Nature Materials, 2004. **3**(10): p. 703-708.
105. Loke, D., et al., *Breaking the Speed Limits of Phase-Change Memory.* Science, 2012. **336**(6088): p. 1566-1569.
106. Chappert, C., A. Fert, and F.N. Van Dau, *The emergence of spin electronics in data storage.* Nature Materials, 2007. **6**(11): p. 813-823.
107. Åkerman, J., *Toward a universal memory.* Science, 2005. **308**(5721): p. 508-510.
108. Chanthbouala, A., et al., *Solid-state memories based on ferroelectric tunnel junctions.* Nature Nanotechnology, 2011. **7**(2): p. 101-104.
109. Garcia, V., et al., *Giant tunnel electroresistance for non-destructive readout of ferroelectric states.* Nature, 2009. **460**(7251): p. 81-84.
110. Gajek, M., et al., *Tunnel junctions with multiferroic barriers.* Nature Materials, 2007. **6**(4): p. 296-302.
111. Guo, R., et al., *Non-volatile memory based on ferroelectric photovoltaic effect.* Nature communications, 2013. **4**: p. 1-5.
112. Zou, X., et al., *Mechanism of Polarization Fatigue in $BiFeO_3$.* ACS Nano, 2012. **6**(10): p. 8997-9004.
113. Zhou, Y., et al., *Mechanism of Polarization Fatigue in $BiFeO_3$: The Role of Schottky Barrier.* Unpublished, 2013.
114. Baek, S.H., et al., *Ferroelastic switching for nanoscale non-volatile magnetoelectric devices.* Nature Materials, 2010. **9**(4): p. 309-314.
115. Li, J., et al., *Ultrafast polarization switching in thin-film ferroelectrics.* Applied Physics Letters, 2004. **84**(7): p. 1174-1176.